Modeling, Control, and Optimization of Autonomous Diesel- and Electric-Powered Off-Highway Vehicles for Energy Efficiency

A DISSERTATION
SUBMITTED TO THE FACULTY OF THE GRADUATE SCHOOL
OF THE UNIVERSITY OF MINNESOTA
BY

Connor P. Edson

IN PARTIAL FULFILLMENT OF THE REQUIREMENTS
FOR THE DEGREE OF
DOCTOR OF PHILOSOPHY

Advisor: Zongxuan Sun

February, 2025

Acknowledgements

I would like to express my gratitude to the group of people who have supported me in creating this dissertation. My advisor, Dr. Zongxuan Sun, provided valuable insight, guidance, and training to make this work possible. His contribution to my development as an academic and a researcher cannot be understated. I would also like to thank the members of my committee, Dr. James Van de Ven, Dr. Kim Stelson, and Dr. Ryan Caverly, for their feedback and support developing this work through a combination of preliminary discussions, meetings, and classes.

I would also like to thank the other members of my lab, current and former, and other colleagues, especially those who have closely worked with me on the autonomous wheel loader project. Gaonan Zhao and Dr. Jie Yao, whose work and advice have helped me get past many roadbloacks during my time here. Dr. Xingyong Song and Sencheng Yu from Texas A&M University, who developed force modeling and linkage tools integral to my work and gave important feedback along the way. Mike Gust, whose engineering experience helped keep the many mathematical models and simulations stay connected to reality.

I would like to acknowledge the funding from the Department of Energy's Office of Energy Efficiency and Renewable Energy (EERE) under the Vehicle Technologies Office Award Number DE-EE0009200 that supported this work. A big acknowledgment also to CNH Industrial for providing financial support, extensive testing data, and technical support from their engineering team.

I am grateful to the members of my program for their support, friendship, and enriching discussions. A special thank you to my fellow engineering graduate students, roommates, and friends Jackson Wills and Jim Gant for their willingness to engage in technical discussions at all hours and for all the shared joy outside research. Thank you

for all that we've done together. To Jackson, thank you for being one of my very first friends in Minnesota. I'm very grateful that we've managed to stick together to the end and for all the help getting through many struggles along the way.

I owe endless thanks to my closest friends, family, and partner. To Casey and Sarah, thank you for helping me grow and for supporting me through the best and worst of grad school. When I needed an escape into the woods or on some other adventure, I am thankful to Casey for always being ready to join me, and to your generous spirit for consistently finding ways to support friends. I am also thankful to Sarah for sharing her humor, her wisdom, and her help in growing significantly as a person during my time here. To Nate and Jax, thank you for helping me keep going from afar and for providing an escape when needed. I take comfort in your presence either on visits, over phone calls, or when listening to the many songs and playlists we've enjoyed together. Thank you to Rue, Elroy, Arrow, Ollie, Charlie, and Ari for quietly providing the emotional support that only a team of animals can.

To my mom and dad, thank you for teaching me to value education enough to come here, and for the unconditional love that helped me stay. Your support means the world to me. I am thankful for the lifelong love of learning you've given me. To my sister Shannon, thank you for always being there, for all the times spent laughing, and for keeping me grounded. I am very lucky to have you as my oldest friend. To my partner Emmy, thank you for picking me back up when I fall, for continually sparking joy, and for the sense of calm you bring. Your steadfast warmth and wisdom is inspiring. Thank you for talking to me about everything and nothing, including much of what follows in this dissertation.

Dedication

To my mom, who lifts me up. To my dad, who taught me to always keep trying.

Abstract

Off-highway vehicles are heavily relied upon for industrial transportation and have highly energy-intensive operation. Automation of off-highway vehicles presents an opportunity to reduce energy consumption without negative impact on productivity through optimization. Prior studies on this topic are lacking a systematic formulation of the optimal control problem for automation. This work introduces novel formulations of the optimal control problem for a typical wheel loader drive cycle for both diesel- and electric-powered vehicles. The formulations include development of control-oriented mathematical models, physical constraints, boundary constraints to create the desired cycle, and multi-objective cost functions. Simulations of the optimized trajectories demonstrate feasibility of implementation and allows deeper analysis of proposed reductions in energy. This work finds that optimal automation for a diesel wheel loader can reduce energy consumption by 42.1% while matching or improving that productivity of a human driver. For electric wheel loaders, this work extends the feasibility of electrification to larger sizes than those found in literature while matching diesel per-day productivity with 1.2 battery charges compared to human drivers and 1.8 battery charges compared to an optimal automated diesel vehicle while demonstrating 74% less energy consumption. The diesel-powered vehicle reduces energy by optimizing the engine operation point via coordination of the driving and working systems, while the electric-powered vehicle further reduces energy consumption with a more efficient architecture. Overall, this work demonstrates the potential for automation of off-highway vehicles to reduce energy consumption, provides a systematic methodology for optimizing automation and evaluating its benefits, and gives a pathway to electrification of mid-size wheel loaders using automation.

Contents

List of Tables

List of Figures

Chapter 1

Introduction

1.1 Background and Motivations

As researchers respond to the global push to increase energy efficiency and decrease fossil fuel emissions, the transportation industry is a major target for improvement. According to the Lawrence Livermore National Lab, transportation accounts for 30% of U.S. energy consumption while powered mostly by fossil fuels, using 70% of the petroleum consumption [2]. In addition, overall energy efficiency for transportation is estimated at only 21%. As worldwide transportation systems aim to increase energy efficiency and sustainability, automation is seen as a tool to achieve better efficiency without sacrificing productivity.

According to Lynch and Zigler, off-highway vehicles accounted for 8% of the U.S. transportation sector's energy consumption [3]. Off-highway vehicles are vehicles which are designed for use in terrain other than public highways and roads, sometimes referred to as off-road vehicles. The term typically refers to motor vehicles with non-passenger applications such as agriculture, construction, or mining. Autonomous off-highway vehicles have been garnering increasing attention from researchers over the last few decades. Off-highway vehicles are energy-intensive and will continue to be widely used. In addition to reducing energy consumption, automation can also help decrease costs and improve safety in fields such as agriculture, construction, and mining.

Off-highway vehicle dynamics are more complex than on-road vehicles because they have another work function in addition to propulsion, which often uses fluid power.

Figure 1.1: CASE 821G Wheel Loader [1]

Internal combustion (IC) engines are widely used as the power source for off-highway vehicles. This work will focus on wheel loaders – which make up a large portion of off-highway vehicle energy consumption – to exemplify off-highway vehicles. Wheel loaders, alongside excavators, are one of the most common off-highway vehicles and are used to transport soil, ore, snow, wood chips, and construction materials in a variety of fields [4]. Wheel loaders have a hydraulic work circuit with a bucket that is powered by the engine in conjunction with the propulsion system. This creates a complex dynamic interaction on the engine shaft, as well as requiring professional operators to handle simultaneous control inputs for driving, steering, and bucket motion.

A mathematical model provides the framework for understanding how the vehicle operates. Since autonomy requires a real-time solution, the model must run quickly while achieving sufficient accuracy to still produce useful results with the major aspects of the vehicle considered. The system model can be divided into subsystems: drivetrain, hydraulic work circuit, and steering, all of which are powered by the engine. Each of these has control inputs that would traditionally be operated by a human: fuel injection (gas pedal), brake torque (brake pedal), bucket tangential and rotational acceleration (valve commands), and steering wheel speed. Gear shifting must be included in the drivetrain model to have accurate results when the loader is transporting material.

Optimization of off-highway vehicle operation is crucial to realizing the major goals of vehicle automation. To replace human operators, autonomous vehicle require guidance on how to complete tasks. Since energy efficiency without loss of productivity is the primary objective, minimizing fuel consumption and cycle time are both of interest. The vehicle must also be sure to fill the bucket completely during each loading to maintain productivity. A formulation that can produce optimal trajectories for complete loading cycles bound to realistic operational constraints with robustness to perturbations and cycle conditions is needed.

To take energy efficiency and sustainability of off-highway vehicles a step further as internal combustion engines and fossil fuels are phased out, they will be electrified. The system model can be adapted to use a battery and electric motors in place of the engine. With this change, wheel loaders can take advantage of the traits of electrical power to separate the drivetrain and hydraulic systems onto two different motors. The battery can also be used for energy storage to reduce energy wasted in braking or excess flow. Electric power, while power-dense, is often limited by its energy-density when applied to electrifying mobile vehicles. Using automation and systematic optimization to improve energy efficiency and productivity will aid electrification of larger vehicles without requiring impossibly large batteries or motors.

While optimization formulations must use control-oriented models with limited order for reasonable computation time and convergence, more accurate high order models are useful in evaluating the feasibility and detailed energy consumption of the optimized trajectory. Simulation of a higher order, validated model will validate and evaluate the proposed optimal results. Control systems must be designed for the relevant systems that will represent automation of the vehicle to track the desired trajectory in simulation. For additional confidence, an existing Hardware-in-the-Loop (HiL) Testbed with a real engine loaded by a dynamometer will be used alongside simulation to evaluate the engine-powered vehicle. This process can be used to adjust the optimal formulation to account for additional losses or unrealistic constraints.

1.2 Literature Review

Automation of off-highway vehicles has been an active area for over four decades [5]. While substantial progress has been made, there are still only limited autonomous off-highway vehicles ready for deployment [6], [7]. Off-highway vehicles, and particularly wheel loaders, typically follow repetitive working cycles that makes them well-posed for automation. Replacing human operators with autonomous off-highway vehicles would bring benefits in cost reduction, safety, and productivity [8]. Dadhich [4] brought forward the technique road map towards fully automated wheel loaders, defining the steps as manual operation, in-sight tele-operation, tele-remote operation, assisted tele-remote operation, and fully autonomous. The current status remains between the tele-remote operation and assisted tele-remote operation. Dadhich also points out the lack of a control-oriented model appropriate for all parts of a short loading cycle and a method to assure performance in regards to fuel efficiency, cycle time, and bucket fill factor.

Autonomous bucket loading is covered by [9, 10] using actor-critic reinforcement learning with a neural networks trained using the trajectories of a human operator. This method can meet cycle time and fill factor requirements for bucket loading, but makes no guarantees on fuel consumption. Autonomous transport is studied in [11], which uses extensive human-driven short loading cycles to determine the optimal driving trajectory based on the orientation of the load receiver and its distance from the loading area.

Optimal trajectory planning can improve upon the trajectories chosen by human drivers and is more generalizable. Optimization has frequently been applied to mobile autonomous systems, as in [12, 13, 14, 15] which solve multi-stage optimization problems for car-like robots and unmanned aerial vehicles. Several previous studies have also covered modeling and optimization of wheel loaders. [16, 17, 18] develops an optimal transport trajectory planning strategy to minimize cycle time and fuel consumption. [19] uses the Genetic Algorithm for optimal transport path planning. [20] uses a random tree algorithm and model predictive control to generate and track a transport path for a linear kinematic model.

Even with potentially significant improvements in fuel efficiency, off-highway vehicles cannot be run sustainably with fossil fuels. Off-highway vehicles have begun to trend towards electrification in recent years as environmental regulations grow stricter and

newer technologies are expected to offer better energy efficiency, lower costs, improved reliability, and increased productivity [21]. Construction vehicles, especially excavators and wheel loaders, are the most commonly electrified off-highway vehicles available, with market shares for both expected to increase significantly in the coming years [22]. However, Beltrami also points out that the state-of-the-art in applications of electric loaders is limited to vehicles under 5000 kg and 30 kW, with power correlating with operating weight [22]. Thus while off-highway electrification is a big area of investment, battery capacity is a limiting factor in electrifying even the larger end of compact loaders. Automation with energy-optimization provides a key pathway to expanding the use of battery-electric wheel loaders.

Until recently, hybrid electric powertrains are most common in off-highway optimal control literature. [23, 24, 25] cover optimal control and energy management for hybrid electric off-highway vehicles with predetermined trajectories. [26] uses MPC to optimize energy management in a hybrid without a pirori knowledge of the trajectory, and [27] is a similar work that uses Pontryagin's minimum principle and considers battery aging.

In the last few years, literature has turned more towards full electrification and automation of compact wheel loaders with encouraging results for energy savings. [28] demonstrates the capability of a small electric forklift to match the productivity of a diesel one while improving efficiency from 25-28% to 77-87%. In [29], Karuppanan simulates the performance of Volvo's autonomous and finds that control design can take advantage of automation to improve efficiency over following human driver behavior, but without systematically optimizing the trajectory. Zhang et al. cover speed trajectory optimization for a battery electric wheel loader in [30]. They combine dynamic programming with Brent's method to improve computation time and optimize battery lifetime. This study only optimizes the speed trajectory during transport phases alone, with fixed waypoints and no consideration of the bucket loading and connection between phases.

Results obtained by solving optimization problems should be validated to support the proposed solution. Simulation of a validated model is commonly used for this purpose in literature. Experimental validation gives an even higher degree of accuracy. [31, 32] propose and use a Hardware-in-the-Loop (HiL) Testbed with a real engine to demonstrate optimal results for connected and autonomous on-road vehicles. This

method is simpler, safer, and less costly than field testing with a full vehicle.

Off-highway vehicles such as wheel loader currently rely on trained human drivers to complete tasks. It is of interest to automate their operation and improve upon human driving abilities by formulating and solving an optimization problem. This requires a control-oriented system model to be used in real-time that covers all parts of a typical loading cycle. Previous studies on modeling and optimization focus on only the transport or bucket loading phases of a cycle alone. None of those that cover transport include gear shifting in their drivetrain models. Creating an optimal formulation that includes all phases of a loading cycle will allow for further improvements in energy efficiency as well as better robustness to cover multiple cycles. Evaluating results from this optimization formulation with simulations and experimentally on an HiL Testbed provides a high degree of confidence in the claimed outcomes. These literature gaps exist for both diesel and electric off-highway vehicles.

1.3 Overview

The objective of the proposed research is to develop a systematic method for the optimization of autonomous off-highway vehicles to save energy, with particular focus on wheel loaders. A control-oriented model for the target vehicle is developed for use in real-time optimization. The optimization problem is formulated with a robust methodology that can apply to a variety of cycles, powertrains, and vehicle models. The results of the optimization will are evaluated with simulations of high order model and experimentally when possible. This research is composed of three parts: diesel optimization formulation, electrification and optimization re-formulation, and result evaluation.

Chapter 2 presents a study on formulation of the optimal control problem for an autonomous diesel-powered wheel loader. The control-oriented model is developed and calibrated using human driving data. The model includes the engine, drivetrain (torque converter, gearbox, driveshaft), work circuit (main pump, bucket, tool-environment interaction), and steering (steering system, vehicle motion dynamics). The optimization problem is formulated with a systematic methodology. A typical loading cycle is defined and converted into a series of constraints that are applied to the problem. The objective function will be defined to reduce energy consumption while maintaining or improving

productivity over human drivers. Physical constraints are applied based on human driving data to keep the vehicle operation in a realistic setting. The methodology for this formulation is robust to changes in the cycle definition and variable constraints. Solving this optimization formulation shows that this methodology can achieve significant gains in energy efficiency without loss of productivity.

Chapter 3 presents a study on electrification for an autonomous wheel loader. A control-oriented electric-powered model is developed for an existing diesel vehicle with minimal changes to the architecture downstream of the power source. Electric components are sized against data for a human-driven cycle of the diesel loader. The optimal control problem formulated in Chapter 2 is adapted and applied for an electric vehicle, along with re-solving the problem for a compact diesel vehicle to directly compare results. Physical and boundary constraints are applied systematically to the new powertrain to maintain a realistic optimization setting considering the battery and motor specifications. Results discussed in this chapter show that the methodology provides a pathway to expanding electrification to larger vehicles using efficiency gains from automation and optimization.

Chapter 4 presents a study on evaluating and validating the optimal cycles created in the two previous chapters. Developing high order, validate system models for a target vehicle using both powertrains with controllers designed to autonomously implement a desired trajectory allows simulation of any developed cycle with detailed analysis of the results. For the diesel vehicle, the results are also evaluated experimentally and discussed using a HiL testbed with a real engine. This study provides a method for evaluating optimal results and reveals how the system's energy efficiency is improved by trajectory optimization. The evaluation provides additional confidence in the feasibility of implementing an optimal autonomous wheel loader, and gives insight on how to further improve the optimization process.

This work is reviewed and has its conclusions summarized in Chapter 5. This chapter provides an overview of the key contributions of this work as a whole and provides recommendations for future work in this area.

Chapter 2

Optimization Problem Formulation of Drive Cycle for an Autonomous Diesel Wheel Loader

2.1 Introduction

This chapter describes the formulation of an optimization problem for a off-highway wheel loader drive cycle. Off-highway vehicle dynamics are more complex than on-road vehicles because they have another work function in addition to propulsion, which often uses fluid power. Internal combustion (IC) engines are widely used as the power source for off-highway vehicles. This work will focus on wheel loaders – which make up a large portion of off-highway vehicle energy consumption – to exemplify off-highway vehicles. Wheel loaders, alongside excavators, are one of the most common off-highway vehicles and are used to transport soil, ore, snow, wood chips, and construction materials in a variety of fields [4]. Wheel loaders have a hydraulic work circuit with a bucket that is powered by the engine in conjunction with the propulsion system. This creates a complex dynamic interaction on the engine shaft, as well as requiring professional operators to handle simultaneous control inputs for driving, steering, and bucket motion.

Automation of off-highway vehicles has been an active area for over four decades [5]. While substantial progress has been made, there are still only limited autonomous

off-highway vehicles ready for deployment [6], [7]. Off-highway vehicles, and particularly wheel loaders, typically follow repetitive working cycles that makes them well-posed for automation. Replacing human operators with autonomous off-highway vehicles would bring benefits in cost reduction, safety, and productivity [8]. Dadhich [4] brought forward the technique road map towards fully automated wheel loaders, defining the steps as manual operation, in-sight tele-operation, tele-remote operation, assisted tele-remote operation, and fully autonomous. The current status remains between the tele-remote operation and assisted tele-remote operation. Dadhich also points out the lack of a control-oriented model appropriate for all parts of a short loading cycle and a method to assure performance in regards to fuel efficiency, cycle time, and bucket fill factor.

Autonomous bucket loading is covered by [9, 10] using actor-critic reinforcement learning with a neural networks trained using the trajectories of a human operator. This method can meet cycle time and fill factor requirements for bucket loading, but makes no guarantees on fuel consumption. Autonomous transport is studied in [11], which uses extensive human-driven short loading cycles to determine the optimal driving trajectory based on the orientation of the load receiver and its distance from the loading area.

Optimal trajectory planning can improve upon the trajectories chosen by human drivers and is more generalizable. Optimization has frequently been applied to mobile autonomous systems, as in [12, 13, 14, 15] which solve multi-stage optimization problems for car-like robots and unmanned aerial vehicles. Several previous studies have also covered modeling and optimization of wheel loaders. [16, 17, 18] develops an optimal transport trajectory planning strategy to minimize cycle time and fuel consumption. [19] uses the Genetic Algorithm for optimal transport path planning. [20] uses a random tree algorithm and model predictive control to generate and track a transport path for a linear kinematic model.

Previous studies on modeling and optimization of wheel loaders focus on only the transport or bucket loading phases of a cycle alone. None of those that cover transport include gear shifting in their drivetrain models. Creating an optimal formulation that includes all phases of a loading cycle will allow for further improvements in energy efficiency as well as better robustness to cover multiple cycles. This study develops a control-oriented model and optimal problem formulation for a CNH 821G Wheel Loader and could be extended to other similar models or alternate set of specifications. The

short loading cycle–also referred to as a Y- or V-shape cycle–will be optimized as a common example for wheel loaders although the formulation can be used to optimize other cycles. The short drive cycle is for a typical loading operation, where the wheel loader is transporting material from a pile to a truck or other collection location.

The optimal control problem formulation developed in this chapter is nonlinear, multi-stage, multi-objective, and time-optimal. Section 2.2.1 introduces the control-oriented model that will be used. Section 2.2.2 gives more detail on the computational aspects used in this chapter. The system model contains nonlinearities that cannot be removed without losing significant accuracy, requiring a nonlinear method. Breaking up the problem into multiple stages discussed in Section 2.2.3 allows the state dynamics and constraints to change between stages to enable implementation of the desired cycle. The objective function in Section 2.2.4 defines the optimality condition. Section 2.2.5 describes the state and control constraints based on physical limitations and 2.2.6 gives the initial and final conditions for each stage that create the cycle, connect the stages, and force the vehicle to achieve the cycle objectives. To the best of the author's knowledge, this is the first systematic formulation of the optimal control problem of a full drive cycle for an autonomous diesel wheel loader.

2.2 Methods

2.2.1 System Model

Fig. 2.1 shows an overview of the system model. The wheel loader is represented by a system model with 13 states and 5 controls. The system states are engine speed ω_e, driveshaft speed ω_d, vehicle x and y position x_p and y_p, heading angle β, steering angle δ, steering angular speed ω_s, bucket x and z position x_b and z_b, bucket tangential and rotational speed v_b and ω_b, bucket orientation α and filled bucket area A_b. The controls are engine fuel injection per cycle u_f, driveshaft brake torque u_d, steering wheel speed u_s, and bucket tangential and rotational acceleration $u_{b,tan}$ and $u_{b,rot}$.

$$x = [\omega_e, \omega_d, x_p, y_p, \beta, \delta, \omega_s, x_b, z_b, v_b, \omega_b, \alpha, A_b]^\mathsf{T}$$
$$u = [u_f, u_d, u_s, u_{b,tan}, u_{b,rot}]^\mathsf{T}$$

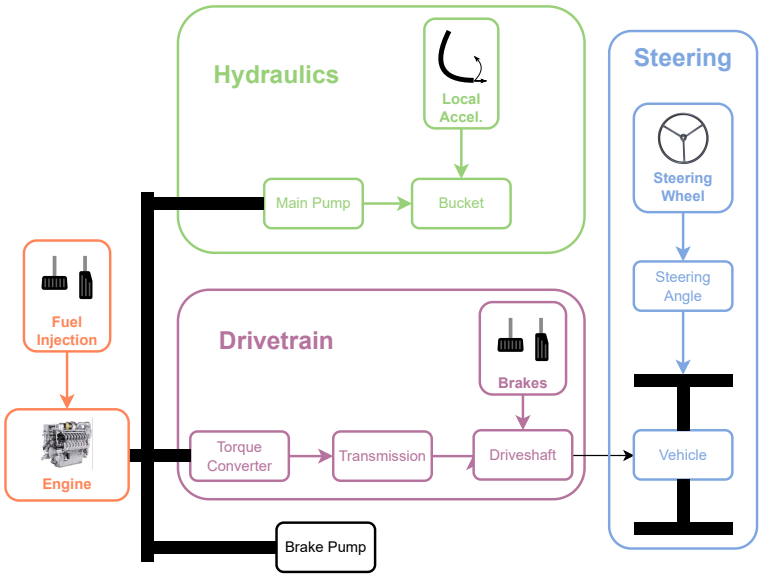

Figure 2.1: Diesel system schematic for control-oriented model

The system model can be broken into three subsystems: the drivetrain, the work circuit, and the steering circuit, all of which are powered by the engine. The engine shaft dynamics are given by

$$\dot{\omega}_e = \frac{1}{J_e}(T_e - T_{tc_p} - T_{mp} - T_{bp}) \tag{2.1}$$

where J_e is the lumped engine shaft inertia. The engine torque T_e is given by Eq. 2.2, the torque converter load T_{tc_p} and main pump load T_{mp} will be analyzed further in this section, and the brake pump torque T_{bp} is considered constant.

$$T_e = \frac{\eta_e q_{hv} n_{cyl}}{4\pi} u_f - \frac{V_d}{4\pi}(c_1\omega_e^2 + c_2\omega_e + c_3) \tag{2.2}$$

where η_e is the engine combustion efficiency, q_{hv} is the lower heating value of diesel fuel, n_{cyl} is the number of cylinders, V_d is the displacement volume, and c_1, c_2, c_3 are calibrated friction coefficients.

The engine fuel consumption is given by

$$\dot{m}_f = \frac{n_{cyl}}{4\pi} u_f \omega_e \tag{2.3}$$

Drivetrain

The drivetrain consists of a torque converter connected to the engine shaft, followed by a transmission gearbox controlled by an automatic shift schedule, and the driveshaft. The torque converter is modeled with the method presented by Kotwicki [33] with the pump torque $T_{tc,p}$ and turbine torque $T_{tc,t}$ given by

$$T_{tc,p} = a_1\omega_e^2 + a_2\gamma\omega_e\omega_d + a_3\gamma^2\omega_d^2 \tag{2.4}$$

$$T_{tc,t} = b_1\omega_e^2 + b_2\gamma\omega_e\omega_d + b_3\gamma^2\omega_d^2 \tag{2.5}$$

where γ is the transmission gear ratio and a_1, a_2, a_3, b_1, b_2, b_3 are calibrated torque converter coefficients.

Gear shifts for the automatic transmission system are determined by a shift schedule that maps vehicle speed and engine throttle to gear shifts [34]. This shift schedule and the resulting gear ratio is discrete, which presents a challenge for nonlinear programming (NLP) solvers relying on a gradient method that requires smooth constraints. To solve this difficulty, the shift schedule mapping is smoothed as in [35]. A piecewise linear function is fit to each curve of the shift schedule. The "distance" (difference between the current speed and the speed at which a shift would occur for the current throttle) from each point on the shift schedule to the nearest curve is stored. A smoothed lookup table can then be computed by a sigmoid function

$$\gamma_k = \frac{\gamma^i - \gamma^{i+1}}{1 + e^{-C\phi(v_k, th_k)}} \tag{2.6}$$

where k is the current timestep, γ^i and γ^{i+1} are gear ratios for consecutive gears, C is a constant that defines the steepness of the function, ϕ is the pre-calculated shift schedule distance function, and th is the engine throttle which is linearly related to fuel injection u_f. Fig. 2.2 shows an example of the resulting map for the 4-speed forward drive with gear numbers rather than gear ratios for readability.

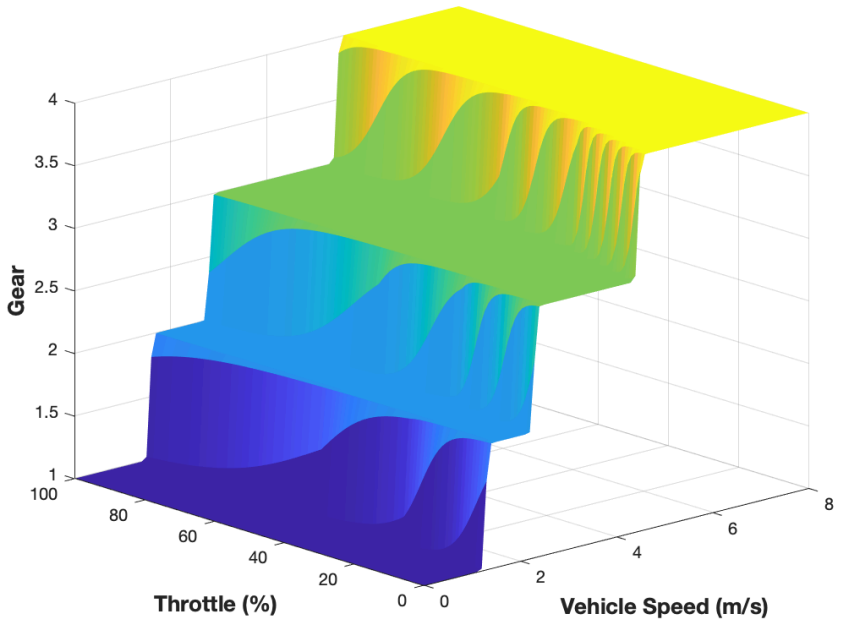

Figure 2.2: Smoothed gear mapping for forward drive

The driveshaft dynamic is given by

$$\dot{\omega}_d = \frac{1}{J_d}(T_d - T_{rr} - T_{pile} - u_d) \tag{2.7}$$

where J_d is the driveshaft inertia and the drive torque T_d, rolling resistance T_{rr}, and pile resistance torque T_{pile} are given by

$$T_d = \gamma T_{tc,t} \tag{2.8}$$

$$T_{rr} = \frac{R_w}{k_f}\mu mg \tag{2.9}$$

$$T_{pile} = \frac{R_w}{k_f}F_h \tag{2.10}$$

where R_w is the wheel radius, k_f is the final drive ratio, μ is the wheel friction coefficient, m is the vehicle mass, g is the acceleration due to gravity, and F_h is the pile resistance force. This force is the horizontal component of the force exerted on the bucket by the pile, which is considered in Section 2.2.1.

The vehicle speed can be calculated by

$$v = \frac{R_w}{k_f}\omega_d \tag{2.11}$$

Work Circuit

The work circuit consumes significant power, particularly when filling and lifting the bucket. A control-oriented model for the work circuit is developed in this section to represent these power requirements and the bucket motion. Model order must be kept low for use in optimization without sacrificing important features. To accomplish this, the pressure and flow dynamics of the hydraulic system are ignored and it is assumed to have a constant (conservatively low) efficiency. The control inputs to the bucket are tangential and rotational acceleration $u_{b,tan}$ and $u_{b,rot}$. The components of bucket velocity are given by

$$\dot{v}_b = u_{b,tan} \tag{2.12}$$

$$\dot{\omega}_b = u_{b,rot} \tag{2.13}$$

The bucket position and orientation is considered in the $x - z$ plane relative to the vehicle position, which can be derived from the tangential-rotational motion as

$$\dot{x}_b = v_b \cos\alpha + R_b\omega_b \cos\psi \cos(\pi - \alpha) - R_b\omega_b \sin\psi \sin(\pi - \alpha) + \dot{x}_p \tag{2.14}$$

$$\dot{z}_b = v_b \sin\alpha - R_b\omega_b \cos\psi \sin(\pi - \alpha) - R_b\omega_b \sin\psi \cos(\pi - \alpha) \tag{2.15}$$

$$\dot{\alpha} = \omega_b \tag{2.16}$$

where R_b is the distance from the bucket tip to the bucket center of mass and ψ is the angle between v_b and $R_b\omega_b$ (assumed constant).

A power balance at the bucket tip and hydraulic pump shaft will give the pump's operating point. The power output by the bucket in the horizontal and vertical directions are

$$P_h = (F_h + m_b g \sin(\pi - \alpha))(v_b + R_b\omega_b \cos\psi) \tag{2.17}$$

$$P_v = (F_v + m_b g \cos(\pi - \alpha) R_b\omega_b \sin\psi \tag{2.18}$$

Then the main pump torque with constant hydraulic circuit efficiency η is expressed as

$$T_{mp} = \frac{P_h + P_v}{\eta \omega_e} \tag{2.19}$$

where m_b is the mass of the bucket and F_h and F_v are found using the fundamental earth-moving equations (FEE), see [36] for details. The FEE model is calibrated and validated by Yu et. al. using human driving data of bucket-pile interaction in [37], although the on-line component of this force model is not suitable for this work. The pile shape must be known and included in the model.

For this work, it is assumed to have a simple parabolic cross-sectional shape shown in Fig. 2.5 and described by

$$z_{pile} = -\frac{3}{4} x_{pile}^2 + 3 x_{pile} \tag{2.20}$$

The area between the pile and the bucket tip trajectory defines the amount of material in the bucket. Eq. 2.21 describes the area dynamic using the differential height difference between the pile and the bucket tip.

$$\dot{A}_b = (-\frac{3}{4} x_{pile}^2 + 3 x_{pile} - z_b) \dot{x}_b \tag{2.21}$$

When there is no bucket-pile interaction–such as during lifting–the bucket typically maintains orientation at its maximum angle with no rotation: $\alpha = \frac{2}{3}\pi$ and $\omega_b = 0$. With these assumptions and no pile resistance forces, the main pump torque can be simplified during lifting:

$$T_{mp} = \frac{(m_b + m_{load}) g v_b \sin(\frac{2}{3}\pi)}{\eta \omega_e} \tag{2.22}$$

Steering

The energy requirements of the steering circuit are low relative to the work circuit, so it is considered negligible. Hence, the steering model is focused on vehicle motion dynamics rather than power demand. The wheel loader vehicle motion can be described using the bicycle model with articulated steering split halfway along the length of the vehicle [17]. The vehicle position and orientation (x_p, y_p, β) can be determined as a

function of steering angle δ and vehicle speed v

$$\dot{x}_p = v\cos\beta \tag{2.23}$$

$$\dot{y}_p = v\sin\beta \tag{2.24}$$

$$\dot{\beta} = \frac{2}{L} v \tan\frac{\delta}{2} \tag{2.25}$$

where L is the vehicle wheelbase. The steering angle is controlled by the steering wheel speed through a series of hydraulic valves and cylinders. The dynamics of the hydraulic steering circuit are approximated with a first-order delay. The time constant is determined by running a step input through a validated full-order model of the vehicle.

$$\dot{\delta} = \omega_s \tag{2.26}$$

$$\dot{\omega}_s = \frac{1}{\tau_s}(-\omega_s + K_s u_s) \tag{2.27}$$

where ω_s is the steering angular speed, τ_s is the time constant of the steering system, and K_s is a scaling constant on the steering wheel speed.

2.2.2 Computational Method

This section describes the computational formulation and solution methodology. The optimization problem is written in MATLAB interfacing with CasADi [38] using IPOPT [39] as the nonlinear programming solver. This formulation uses the Gauss pseudospectral numerical method for multi-stage optimal control as described in [40]. Using this method allows the cycle stages in the next section to join together and optimize across them all at once. It is well-suited for including a lookup table representing the drivetrain shift schedule which introduces a steep gradient under certain operating conditions. It also allows for a time-optimal solution such that the objective function of Section 2.2.4 is usable.

To formulate and solve the problem numerically, this method discretizes the cost function and differential, and algebraic equations during each stage, then connects the time and states between each stages to ensure continuity. The control variables can be set at each time step with the states interpolated between steps using third order Lagrangian collocation. This creates a cubic spline approximation of the state derivative

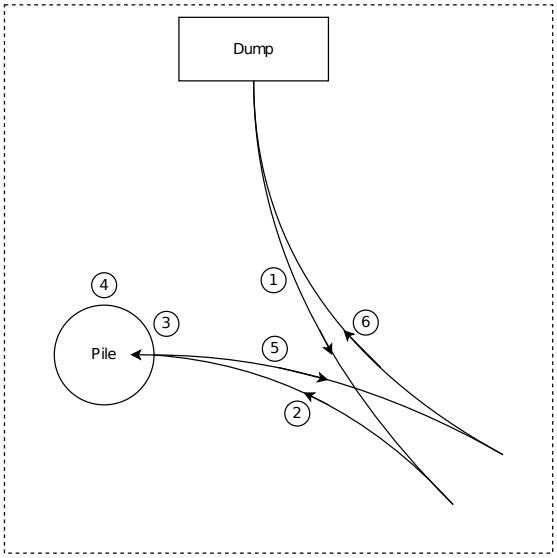

Figure 2.3: Short (V-shape) loading cycle

between steps to allow fewer time steps for each stage while maintaining accuracy.

2.2.3 Cycle Definition

The optimization problem to solve represents a typical short loading cycle. The wheel loader travels from the dump site to the material pile, fills the bucket, and travels back to the dump site while lifting the bucket in preparation to unload. This cycle can be broken into six stages, described in Table 3.1 and shown in Fig. 2.3. Table 3.1 also shows how these six stages can be paired into three phases with similar dynamics and cycle objectives.

Separating the transport and bucket loading phases allows unnecessary states and controls to be eliminated from the dynamics of each stage to reduce model order. During the transport phases, bucket orientation need not change, bucket motion in the x direction is negligible during lifting, and the bucket filled area cannot change, so x_b, ω_b, α_b, A_b, and $u_{b,rot}$ are not considered. Similarly, steering does not occur during the bucket loading phase where the vehicle is assumed to drive straight along the x axis with heading angle $\beta = \pi$ and no motion in the y direction, so y_p, δ, ω_s, β, and u_s are not considered. While both bucket loading and transport with lifting phases contain

Table 2.1: Short cycle phase and stage breakdown

Phase	Stage
Transport 1	1. Reverse 1 2. Forward 1
Bucket Loading	3. Digging 4. Stationary Digging
Transport 2	5. Reverse 2 (lifting) 6. Forward 2 (lifting)

bucket motion, the forces on the bucket are different. During bucket loading these forces come from interaction with the material pile as it pushes back on the bucket. When out of the pile and lifting, the bucket only experiences forces due to gravity acting on the bucket and its material.

Each phase is split into a pair of stages delineated by a change in the state dynamics. The separate reverse and forward stages allow the direction of travel to change within the vehicle dynamics. The two digging stages prescribe that the vehicle will first drive into the pile, then come to a stop as it finishes filling the bucket without driving into the resistance forces from the pile. Each stage has 15 time steps.

The three phases are first solved separately before considering the full multi-stage optimal control problem. This separate solution need not be obtained chronologically. The bucket loading phase is solved first with fewer boundary constraints, and its initial and final states are used to constrain the boundaries of the first and second transport phases for continuity. The resulting solution has optimal behavior within each phase and matching boundary conditions, but has not been optimized across all phases together. This partially combined optimal solution is used as an initial guess to warm-start the solution for the fully combined optimization problem, wherein all phases/stages are formulated and solved together. This solution method improves computation time and convergence of the full solution.

2.2.4 Objective Function and Problem Definition

Since both maximizing productivity and minimizing fuel consumption are important in wheel loader operation, a multi-objective optimization problem is considered. Cycle

time is used as a measure of productivity wince each cycle will transport a consistent quantity of material. Each term in the cost function J is normalized and weighted according to the desired emphasis on the objectives with $w_1+w_2=1$. The normalization terms T_{norm} and $m_{f,norm}$ are defined as the average cycle time and fuel consumption for a human driver based on experimental data. The bucket fill factor is included as a constraint to ensure that the bucket is completely filled in each cycle. The multi-stage optimal control problem can be formulated as

$$\min_{x^{(s)},u^{(s)},t_f^{(s)}} \quad J=\sum_{s=1}^{6} w_1\frac{t_f^{(s)}}{T_{norm}}+w_2\frac{m_f^{(s)}}{m_{f,norm}} \tag{2.28}$$

$$\text{subject to :} \qquad \dot{x}^{(s)}=f^{(s)}(x^{(s)},u^{(s)}), \qquad (s=1,...,6) \tag{2.29}$$

$$x_{min}^{(s)}\le x^{(s)}\le x_{max}^{(s)}, \qquad (s=1,...,6) \tag{2.30}$$

$$u_{min}^{(s)}\le u^{(s)}\le u_{max}^{(s)}, \qquad (s=1,...,6) \tag{2.31}$$

$$h^{(s)}(x^{(s)},u^{(s)})\le 0, \qquad (s=1,...,6) \tag{2.32}$$

$$g^{(s)}(x^{(s)},u^{(s)})=0, \qquad (s=1,...,6) \tag{2.33}$$

$$x^{(s+1)}(t_0^{(s+1)})=x^{(s)}(t_f^{(s)}), \qquad (s=1,...,5) \tag{2.34}$$

where s is the stage number, the dynamic equations in Eq. 2.29 are described in Chapter 2.2.1, Eqs. 2.30 and 2.31 are the state and control bounds, Eq. 2.32 are the inequality constraints, Eq. 2.33 are the equality constraints, and Eq. 2.34 links the stages by constraining the initial and final states of adjacent stages to be equal. The final time of each stage is considered as an additional optimization variable. Optimization occurs over the state variables $x^{(s)}$, control variables $u^{(s)}$, and the final time $t_f^{(s)}$ of each stage.

2.2.5 Physical Constraints

Physical constraints included in the optimal control problem present a realistic setting for wheel loader operation. The following constraints are drawn from human driving

data for the modeled vehicle. Eqs. 2.30 and 2.31 limit the state and control to operate within feasible ranges. In addition to these direct constraints on state and control variables, the inequality constraints in Eq. 2.32 include limitations on algebraic combinations of states and control detailed below.

Engine torque (Eq. 2.2) and main pump torque (Eq. 2.19) are limited by the capabilities of the engine and pump.

$$T_e - T_{e,max} \leq 0 \tag{2.35}$$

$$T_{mp} - T_{mp,max} \leq 0 \tag{2.36}$$

$$\tag{2.37}$$

There is also a terminal constraint on the second digging stage that forces the bucket tip to be somewhere on the edge of the pile described by Eq. 2.20 when bucket loading is completed. The particular bucket tip height and depth are not specified and can be determined by the optimization, but it must be on the pile boundary to be ready to leave the pile.

$$z_b(t_f^{(4)}) + \frac{3}{4}x_b(t_f^{(4)})^2 - 3x_b(t_f^{(4)}) = 0 \tag{2.38}$$

Polack shows that the bicycle model is accurate while the lateral acceleration a_{lat} is less than $0.5\mu_p g$ [41] where μ_p is the peak road friction coefficient. This constraint is not included in the problem formulation because it is unnecessary: the lateral acceleration is always well below this value due to the limits on steering angle and vehicle speed and acceleration. Satisfaction of this criterion is shown with results in Section 2.3. The vehicle lateral acceleration is

$$a_{lat} = \frac{2}{L}v^2 \tan(\delta/2) \tag{2.39}$$

2.2.6 Boundary Constraints for Integration of the Multi-stage Optimization

Boundary constraints are designed for the initial and final states for each stage so that the multi-stage optimization problem can be seamlessly integrated. For each stage, the initial states must match the final states of the previous stage. These constraints–summarized in Table 2.2–define the short loading cycle shown in Fig. 2.3. The engine

Table 2.2: State constraints at initial (i) and final (f) boundaries of each stage

Stage:	Reverse 1		Forward 1		Digging		Stat. Digging		Reverse 2		Forward 2	
State	i	f	i	f	i	f	i	f	i	f	i	f
ω_e	$\omega_{e,0}$	–	–	–	–	–	–	–	–	–	–	$\omega_{e,0}$
ω_d	0	0	0	–	–	0	0	0	0	0	0	0
x_p	-4	–	–	0	0	–	–	–	–	–	–	-4
y_p	-11	–	–	0	0	0	0	0	0	–	–	-11
β	π	–	–	$\frac{\pi}{2}$	$\frac{\pi}{2}$	$\frac{\pi}{2}$	$\frac{\pi}{2}$	$\frac{\pi}{2}$	$\frac{\pi}{2}$	–	–	π
δ	0	–	–	0	0	0	0	0	0	–	–	0
ω_s	0	–	–	0	0	0	0	0	0	–	–	0
x_b	–	–	–	–	-4	–	–	–	–	–	–	–
z_b	0	0	0	0	0	–	–	–	–	–	–	5
v_b	0	0	0	0	0	–	–	–	–	–	–	0
ω_b	0	0	0	0	0	–	–	0	0	0	0	0
α	π	π	π	π	π	–	–	–	–	–	–	–
A_b	0	0	0	0	0	–	–	1	1	1	1	1

speed ω_e at the beginning and end of the cycle must match to ensure there is no extra initial energy injected. The vehicle position and orientation (x_p, y_p, β) define the locations of the dump site and the material pile. The driveshaft speed ω_d goes to zero whenever the vehicle must come to a stop to switch directions or for stationary digging. The steering angle δ and angular speed ω_s are zero when the vehicle should be driving straight longitudinally. The bucket horizontal position x_b is only specified to define the pile location and is not considered during transport phases. Bucket vertical position z_b begins at zero to start loading the bucket and must finish the cycle at the maximum height for dumping. The bucket tangential and rotational speeds v_b and ω_b are zero outside of bucket loading and lifting. The bucket orientation α is flat to the ground as it approaches the pile. Finally, the filled bucket area A_b goes from empty to full during the bucket loading phase, which guarantees a maximized bucket fill factor for each cycle.

The states unconstrained at the boundary provide potential opportunities for optimization, such as the vehicle position and steering angle between each transport stage, the driveshaft speed between the first transport phase and bucket loading phase, the

engine speed between each stage, and the bucket height and speed at the end of the stationary digging and between the second transport stages.

For example, the optimal driveshaft speed when transitioning from transport to bucket loading depends on both phases: For the transport phase, slowing down wastes both time and energy due to braking while acceleration requires generating power from the engine. In the bucket loading phase, there must be a balance between using the drivetrain to quickly and efficiently plunge into the pile without digging too deep and wasting energy lifting excess material that will not ultimately fit inside the bucket. Kinetic energy from the transport phase can be converted directly into mechanical energy by filling the bucket during loading. This optimal boundary speed that uses the least amount of energy and cycle time while filling the full bucket is left to the solver to determine mathematically, along with the other listed boundary states. These benefits can only be obtained when the stages are integrated into the multi-stage optimization framework.

2.3 Results and Discussion

Results from the proposed optimal control problem are presented in this section.

Fuel consumption and cycle time are presented with a range of weights w_1 and w_2 from Eq. 2.28 in Table 2.3. The percent difference columns are compared to the experimental data of a human operator, which show that the performance can be significantly improved by optimization. The cost weight variation shows that there is little benefit to be gained from heavily emphasizing fuel savings over productivity. However, placing a heavy emphasis on productivity over fuel savings can lead to a faster cycle time while still saving fuel compared to a human driver. This formulation allows this trade-off to be controlled according to the desired conditions of operation. Detailed time series of optimal results are shown for the balanced case of $w_1 = 0.5, w_2 = 0.5$.

There are two major ways in which the optimal results are able to save energy compared to a human driver: optimizing the engine operating point and shortening travel distances. Fig. 2.4 shows the engine speed and torque. Engine speed is kept low when possible, dropping quickly during the second half of each transport stage. The engine torque typically runs at either high torque (high efficiency) or low torque (low

Table 2.3: Optimization results

Cost Weights	Time (s)	(%) Diff	Fuel (g)	(%) Diff
$w_1 = 0.5, w_2 = 0.5$	28.2	2.1%	121	42.1%
$w_1 = 0.01, w_2 = 0.99$	40.7	-41.3%	113	45.9%
$w_1 = 0.99, w_2 = 0.01$	25.4	11.8%	159	23.9%
Human	28.8	–	209	–

power) to avoid any low efficiency, high power cases. The bucket loading phase has a high power demand, and engine torque stays high while engine speed remains relatively low.

The vehicle trajectory during each phase is shown in Fig. 2.5. Travel distance is minimized by curving the transportation trajectory, which benefits both components of the cost function. The flatter, horizontal shape at the end of Transport 1 with a longer forward stage enables to vehicle to hit the optimal velocity when plunging into the pile at the boundary between transport and loading. The shape of Transport 2 is more even between stages and covers a longer total distance than the first phase as it is influenced by the demands of the lifting requirement shown later in this section.

Fig. 2.5 also shows the bucket loading trajectory within the pile cross-section. The bucket is filled by first driving straight into the pile with the bucket on the ground, then rotating the bucket and pulling up through the pile vertically. The depth that the bucket plunges is important for minimizing energy, and heavily reliant on coordinating the vehicle speed at the end of transport and coming into the pile, which is only possible with an optimized autonomous system.

Further results for the drivetrain are shown in Fig. 2.6. The vehicle is driven aggressively for fast transport and quickly shifts up to second or third gear depending on the length of the transport stage. Rather than coming to a stop at the beginning of the bucket loading phase, the vehicle plunges into the pile with some remaining speed and uses the resistance force to decelerate. It then remains stationary as the bucket finishes filling to avoid wasting energy through the drivetrain. The difference between Transport 1 and Transport 2 is shown again by the difference in gears used and speeds reached as the hydraulic system demands power when lifting. Engine speed is kept low to limit fuel consumption when high power is not needed.

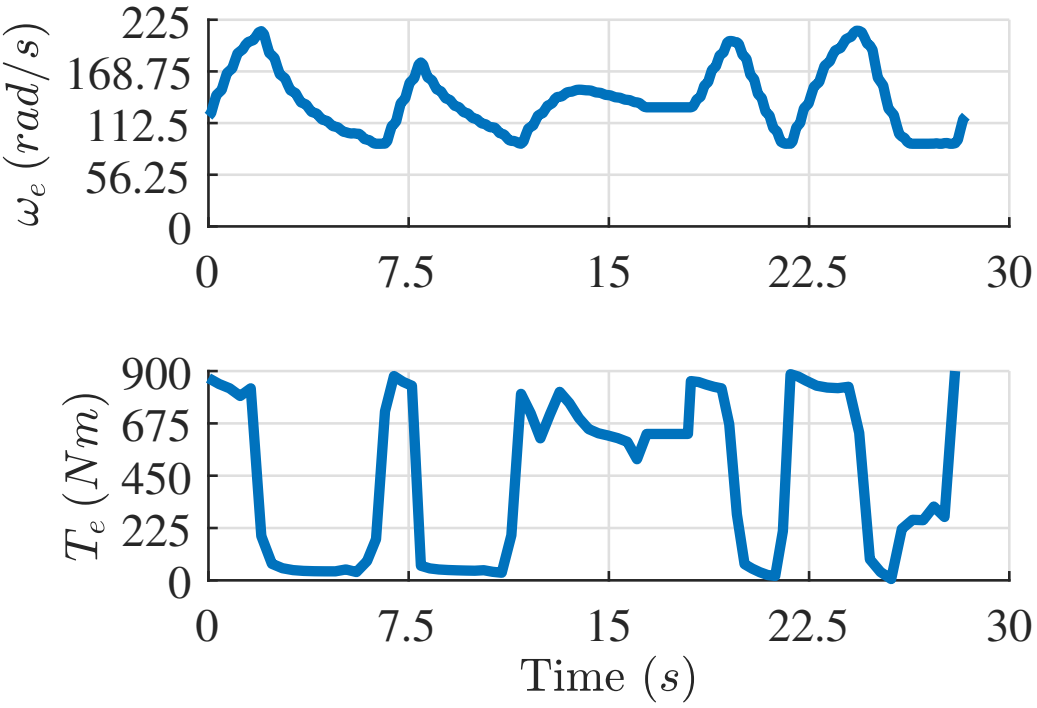

Figure 2.4: Engine speed and torque

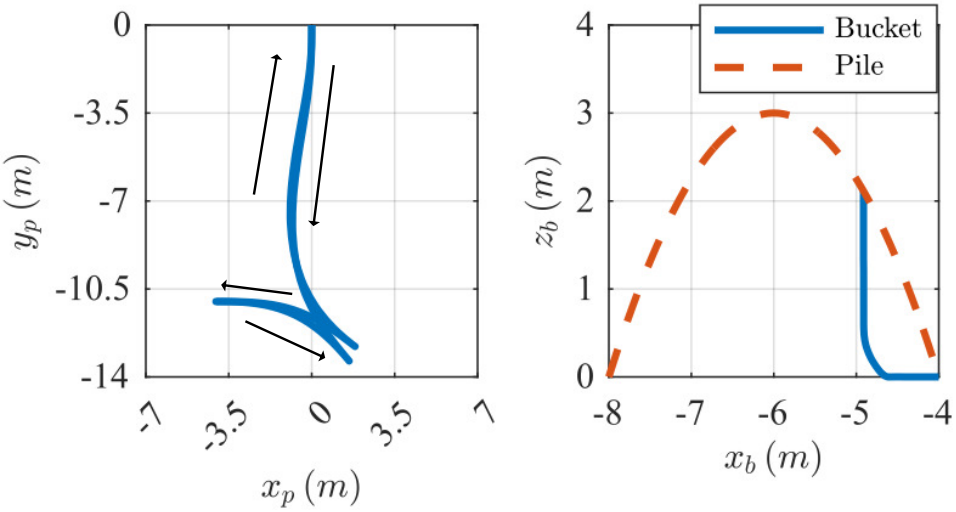

Figure 2.5: Vehicle trajectory across cycle

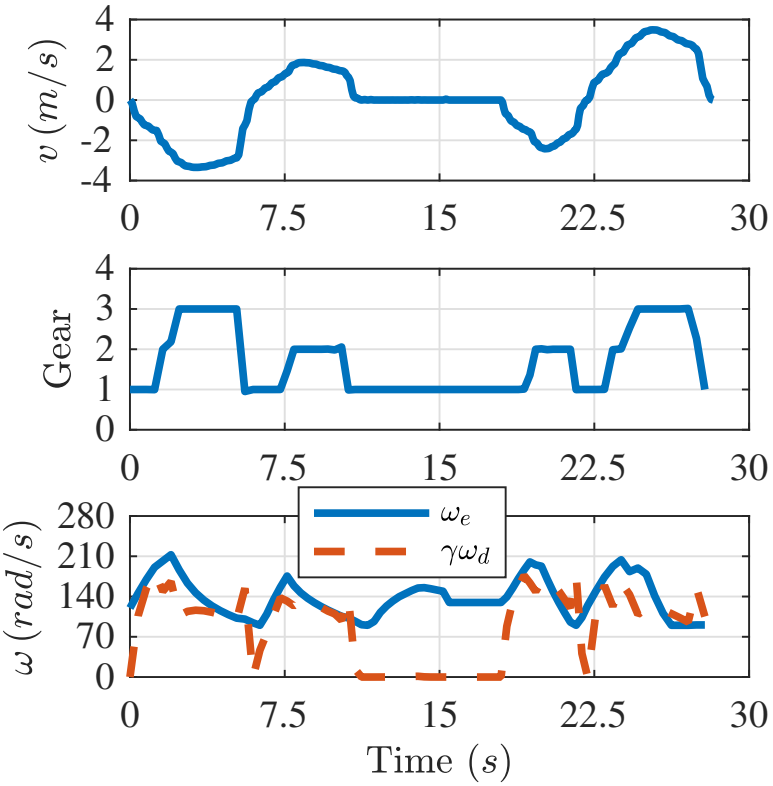

Figure 2.6: Drivetrain results: engine speed, vehicle speed, and gear command

Fig. 2.7 shows how the curvature seen in the transport trajectory was produced. The vehicle is steering at maximum speed at nearly all times during transport to reduce travel distance as much as possible.

Fig. 2.8 shows how the bucket moves through the pile during bucket loading and subsequently lifting during the second transport phase. The bucket moves quickly during bucket loading in coordination with its rotation and the vehicle driving into the pile to get the desired bucket loading trajectory. Afterwards, the bucket completes the lift in two parts at the end of each transport stage. By lifting when the vehicle needs to decelerate, the main pump can help pull the engine speed down to save additional energy otherwise wasted through braking. The bucket orientation begins flat against the ground when plunging into the pile then quickly tilts back to vertical for the rest of the cycle.

For this solution to be used in real-time as a reference for an automated wheel loader, it must be able to recompute the optimal solution for the next cycle before completing the current cycle. The separate phase solution used to generate an initial guess can be solved offline. The computation time for these results for the fully combined cycle was 16.5 seconds on a MacBook Pro with Intel i5 core, 8 GB RAM. A more powerful real-time controller would be used in implementation, which could further increase computational speed. Since this is significantly less than the cycle time of 28.2 seconds, this formulation can be used for real-time operation.

2.4 Conclusion

In this chapter, a novel formulation for multi-objective optimization of an automated wheel loader short cycle including both the transport and bucket loading phases is proposed. The proposed framework can be applied to other similar vehicles or cycles and is flexible to adjustments in model parameters, constraints, and cost weighting. A control-oriented model for both phases is developed to facilitate the model-based optimization design. The system model incorporates an automatic gear shift schedule for the first time. With the selection of the appropriate physical constraints and performance indexes, the optimization results show that the proposed strategy is effective in reducing fuel consumption by 42.1% and has the potential to be incorporated into automated

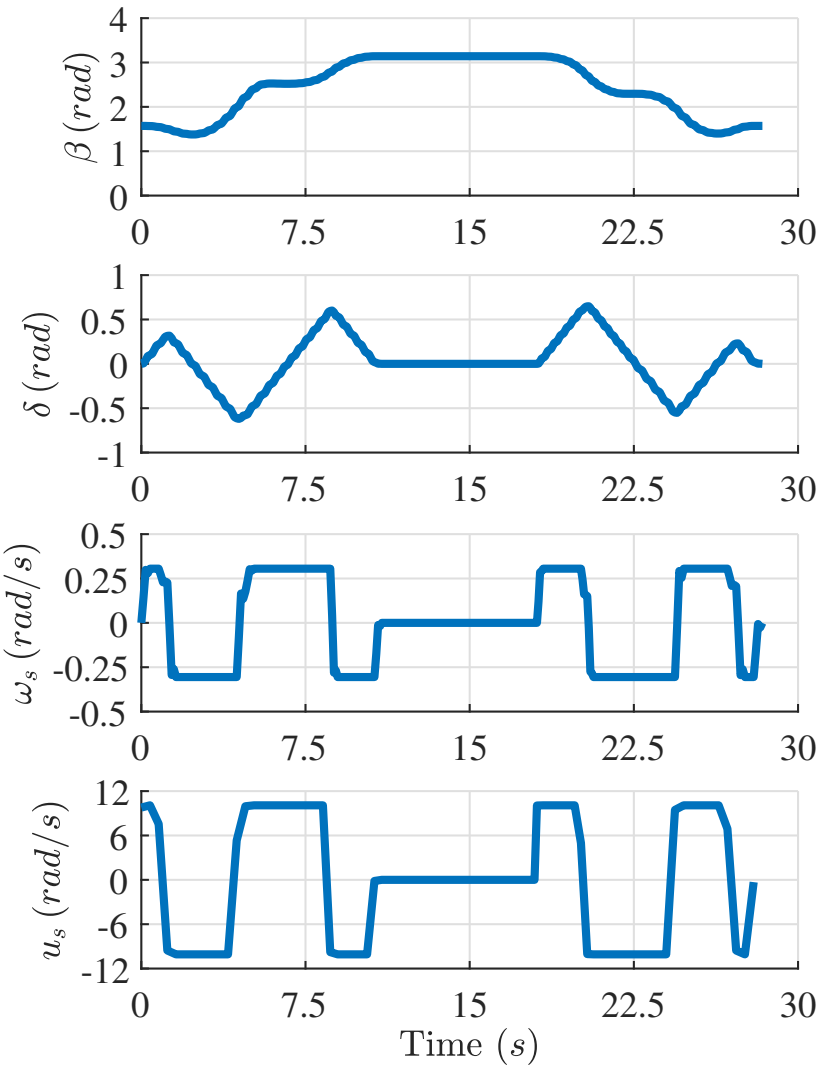

Figure 2.7: Steering results: heading angle, steering angle, steering angular speed, and steering wheel speed

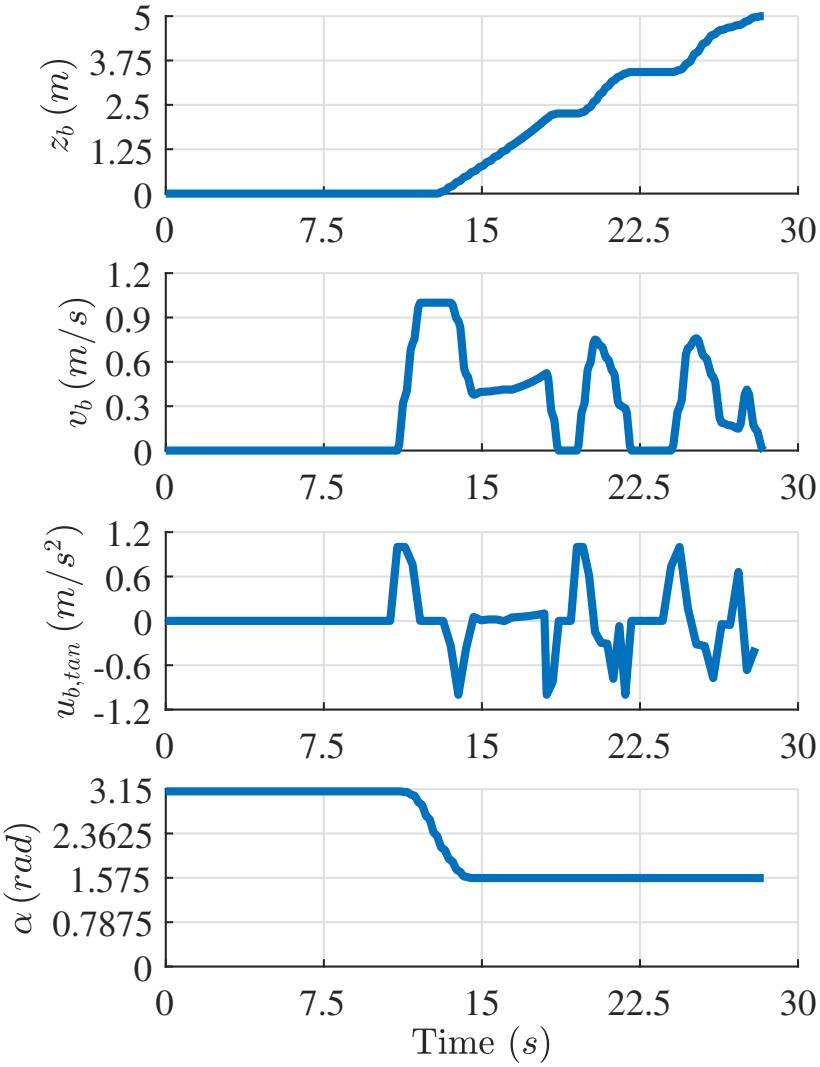

Figure 2.8: Bucket tip motion: height, tangential speed, tangential acceleration, and orientation

wheel loader control. The results of solving this optimal control problem can be analyzed in more detail with a simulation of a high order model. A Hardware-in-the-Loop testbed is being built as well for further study. To demonstrate the robustness of this formulation method, it should be applied to different cycles and vehicle models.

Chapter 3

Electrification and Optimization Problem Formulation for an Autonomous Wheel Loader

3.1 Introduction

This Chapter presents a study on electrification of a compact (mid-size) wheel loader while formulating the optimal control problem for an electric powertrain. Even with potentially significant improvements in fuel efficiency, off-highway vehicles cannot be run sustainably with fossil fuels. Off-highway vehicles have begun to trend towards electrification in recent years as environmental regulations grow stricter and newer technologies are expected to offer better energy efficiency, lower costs, improved reliability, and increased productivity [21]. Construction vehicles, especially excavators and wheel loaders, are the most commonly electrified off-highway vehicles available, with market shares for both expected to increase significantly in the coming years [22]. While electric vehicle development for passenger cars is reasonably mature, the literature on applying the technology to off-highway vehicles is more scarce [42]. The primary limiting issue in electrification of wheel loaders is energy storage. Diesel fuel has much denser energy storage than electric batteries and refueling is much faster than recharging a battery [43]. Because of this difference, off-highway vehicle electrification is currently focused

on small to medium size vehicles [22].

Since electric off-road vehicles are still under development, trends have not yet been fully solidified. Hybrid electric vehicles are considered the most viable option in the short-term, but fully electrified vehicles are expected to gain popularity as technological barriers are overcome [42]. Even among fully electrified off-road vehicles, there are a variety of proposed designs. For electric excavators, it is common to simply swap out the IC engine with a battery and electric motor of equivalent power, while wheel loaders most commonly use a battery with two motors to separate the drivetrain and hydraulic subsystems [22]. This wheel loader architecture is popular because it can increase system efficiency and productivity by avoiding unnecessary losses caused by competing subsystem demands. With drivetrain design in wheel loaders, it is also important consider the strengths and weaknesses of battery power compared to IC engine power – while IC engines are most efficient at lower speeds, a battery and electric motor can provide peak electrical power at a wide range of speeds without loss of efficiency [44]. With this consideration, a drivetrain with an automatic transmission and torque converter may not be necessary with an electrified powertrain.

Until recently, hybrid electric powertrains are most common in off-highway optimal control literature. [23, 24, 25] cover optimal control and energy management for hybrid electric off-highway vehicles with predetermined trajectories. [26] uses MPC to optimize energy management in a hybrid without a pirori knowledge of the trajectory, and [27] is a similar work that uses Pontryagin's minimum principle and considers battery aging.

In the last few years, literature has turned more towards full electrification and automation of compact wheel loaders with encouraging results for energy savings. [28] demonstrates the capability of a small electric forklift to match the productivity of a diesel one while improving efficiency from 25-28% to 77-87%. In [29], Karuppanan simulates the performance of Volvo's autonomous and finds that control design can take advantage of automation to improve efficiency over following human driver behavior, but without systematically optimizing the trajectory. Zhang et al. cover speed trajectory optimization for a battery electric wheel loader in [30]. They combine dynamic programming with Brent's method to improve computation time and optimize battery lifetime. This study only optimizes the speed trajectory during transport phases alone, with fixed waypoints and no consideration of the bucket loading and connection between

phases.

However, Beltrami also points out that the state-of-the-art in applications of electric loaders is limited to vehicles under 5000 kg and 30 kW, with power correlating with operating weight [22]. Thus while off-highway electrification is a big area of investment, battery capacity is a limiting factor in electrifying even the larger end of compact loaders. Automation with energy-optimization provides a key pathway to expanding the use of battery-electric wheel loaders.

This chapter will discuss electrification and automation of a Compact Wheel Loader as an example. This vehicle has an operating weight of about 11,000 kg and engine power rating of 120 kW. The optimization formulation developed in Chapter 2 will be adapted appropriately for an electric powertrain and smaller vehicle. Appendix A.1 contains the model parameters for this vehicle along with the electric powertrain specifications developed in Section 3.2.1. To the best of the author's knowledge, this is the first systematic formulation of the optimal control problem of a full drive cycle for an autonomous electric wheel loader.

3.2 Methods

3.2.1 Electric System Model

To electrify the wheel loader powertrain, the engine must be replaced with a battery and electric motor(s). Since the properties of electric energy storage and power generation differ from that of diesel fuel, the architecture of the electric system need not be identical. This following subsections develop the architecture design, state dynamics, and component sizing for an electric wheel loader powertrain.

Architecture Design

This work will consider an electric powertrain architecture that takes advantage of the properties of electric power and energy storage without introducing excessive complexity to the system. A battery stores all the energy for the system and discharges power to the motors. Using two electric motors, the powertrain is split between the drivetrain and the hydraulic circuit. Each PMSM motor is connected to an inverter that converts

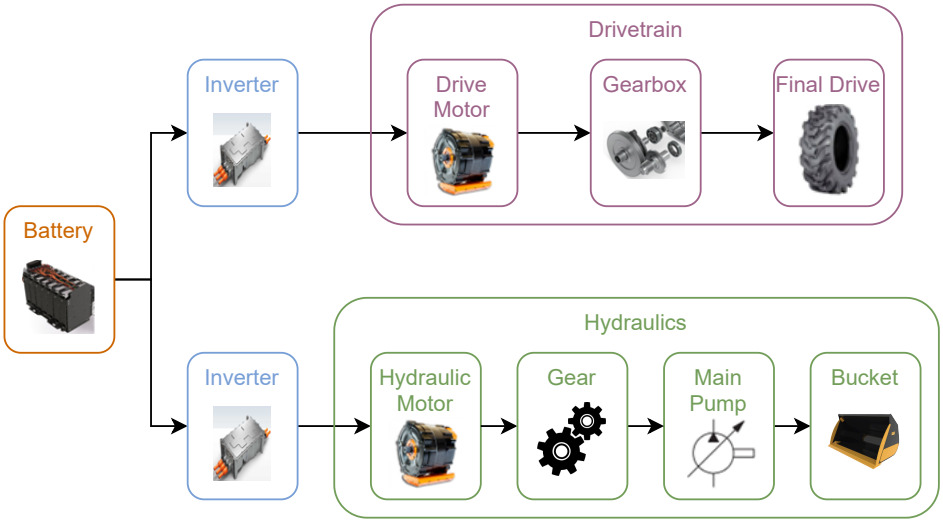

Figure 3.1: Electric wheel loader architecture

the battery's power discharge into AC power to run the motors. Fig. 3.1 summarizes this design.

For the drivetrain, the transmission needs only two speeds due to the electric motor's ability to maintain high efficiency across a wide range of speeds. Many EV applications use a single fixed-gear transmission for this reason, but the wheel loader has competing needs to perform both transport and loading that impact motor operating conditions. During transport, the motor needs to be capable of propelling the vehicle to move quickly (high speed, low torque), while during loading the motor must overcome large loads from interaction with the material pile (low speed, high torque). With a two-speed transmission, the motor can be sized for the power demands of the cycle while the transmission converts that power to the necessary operating point.

The hydraulic circuit itself is unchanged from the diesel-powered model. An electric motor is connected to the main hydraulic pump through a fixed gear. Since the main pump is the same as the one in the diesel model, it is designed to receive power at relatively low speeds and high torques – which is an efficient operating point for an engine. The electric motor and battery are most efficient at high speeds and torques, so the fixed gear between motor and pump converts between these desired operating

points.

One of the most important aspects of energy efficiency in an electric powertrain is the ability to regenerate energy. Regenerative braking is commonly used in EVs and will be used in this design to recapture kinetic energy by sending current back to the battery. There is also potential to regenerate energy from the hydraulic circuit when lowering the bucket, but this requires replacing the hydraulic main pump with a pump-motor to recapture this potential energy. For the scope of this work, hydraulic regeneration will not be considered since it complicates the circuit design for much less benefit compared to regenerative braking.

State Dynamics

This section describes the dynamic system model used in formulating the electric wheel loader optimization problem with the architecture described in the previous section. The full system has 14 states x and 6 controls u with each phase considering only the necessary variables to reduce complexity. Most states and controls are identical to the diesel system of Chapter 2 and will not be repeated here. The differences come in the powertrain: electrical states SOC, ω_d, ω_h and controls u_d, u_h replacing fuel consumption, engine speed and fuel injection. Motor output torque is the control variable for the electric motors.

$$x = [SOC, \omega_d, \omega_h, x_p, y_p, \beta, \delta, \omega_s, x_b, z_b, v_b, \omega_b, \alpha_b, A_b]^\mathsf{T}$$
$$u = [u_d, u_h, u_{br}, u_s, u_{b,tan}, u_{b,rot}]^\mathsf{T}$$

Electric power dynamics are given by:

$$\dot{SOC} = -\frac{V_{bat} - \sqrt{V_{bat}^2 - 4R_{bat}P_{em}}}{2R_{bat}} \tag{3.1}$$

$$\dot{\omega}_d = \frac{1}{J_d}(T_d - T_{br} - T_{rr} - T_{pile} - b_d\omega_d) \tag{3.2}$$

$$\dot{\omega}_h = \frac{1}{J_h}(T_h - \frac{T_{mp}}{\gamma_h} - b_h\omega_h) \tag{3.3}$$

with total input electric motor power P_{em} and motor loss for $i = d, h$

$$P_{em} = T_d\omega_d + loss_d + T_h\omega_h + loss_h \tag{3.4}$$

$$loss_i = P_{max,i}\left(p_1\left(\frac{T_i}{T_{max,i}}\right)^2 + p_2\left(\frac{\omega_i}{\omega_{max,i}}\right)^2 + p_3\frac{T_i}{T_{max,i}}\frac{\omega_i}{\omega_{max,i}} + p_4\right) \tag{3.5}$$

During regenerative braking, the drive motor torque is negative, which flips the sign of motor power and causes the SOC to increase, representing the recaptured energy as the motor sends current back to the battery. Motor loss is used for better numerical stability than efficiency. The SOC dynamic equation implicitly includes a resistance model for battery losses, which are proportional to the square of discharge current or power, and the inverter converting the motor's high current draw and lower voltage to the battery voltage and necessary current discharge. For all other state dynamics and algebraic equations, see Section 2.2.1 Eqs. 2.10-2.27 substituting a mode-based fixed gear for the transmission torque converter and shift schedule and inserting a fixed gear ratio between the hydraulic pump and its electric motor. The constant model parameters are summarized in Appendix A.1.

Work Circuit Constraints

While this model neglects the hydraulic dynamics, there are physical limitations on bucket motion that must be considered. Both the speed of bucket motion and its displacement will require constraints to maintain feasibility. This is especially important when the hydraulic circuit is driven by its own motor, since there is nothing else requiring speed to be sufficiently high. A relationship between bucket tip velocities and required flow will be necessary to create desired motion. Bucket speed is produced by flow generated at the main pump, and the flow available is limited by the pump displacement and speed:

$$Q_{mp} = \frac{D_{mp}}{\gamma_h}\omega_h \tag{3.6}$$

Total flow required by the hydraulic circuit combines work circuit and steering circuit flow demand:

$$Q_{req} = Q_w + Q_s \tag{3.7}$$

The flow required by the work circuit is given by the lift and tilt cylinder speeds

$$Q_w = A_{lift} v_{lift} + A_{tilt} |v_{tilt}| \tag{3.8}$$

The linkage mechanism between the bucket tip and hydraulic cylinders is too complex to fully include, but can be approximated with constant parameters p_l, p_t calibrated against the Lagrangian mechanism model developed in [45]. The lift cylinder velocity can be considered proportional to the bucket tangential velocity, with the tilt cylinder velocity proportional to the bucket rotational velocity:

$$v_{lift} = p_l v_b \tag{3.9}$$

$$v_{tilt} = p_t \omega_b \tag{3.10}$$

Steering circuit flow is modeled as proportional to the steering speed, with the parameter p_s calibrated using a high order hydraulic circuit model from [46]:

$$Q_s = p_s |\omega_s| \tag{3.11}$$

The linkage mechanism also determines the spacial boundary that the bucket tip can reach through the range of possible cylinder displacements. The bucket tip typically follows curving motions: as the bucket extends away from the vehicle it also lifts off the ground. Fig. 3.2 shows a scatter of all feasible bucket positions and a curve fit of the boundary given by Eq. 3.12. The x-axis is horizontal bucket position isolated from vehicle motion ($x_b - x_p$).

$$z_{b,min} = p_{b1}(x_b - x_p)^2 + p_{b2}(x_b - x_p) + p_{b3} \tag{3.12}$$

Component Sizing

The electrified system requires sizing the battery, electric motors, and gear ratios to complete the model. Using data from a human-driven cycle with a diesel version of the target wheel loader, the vehicle speed and load from the bucket material and pile pushing

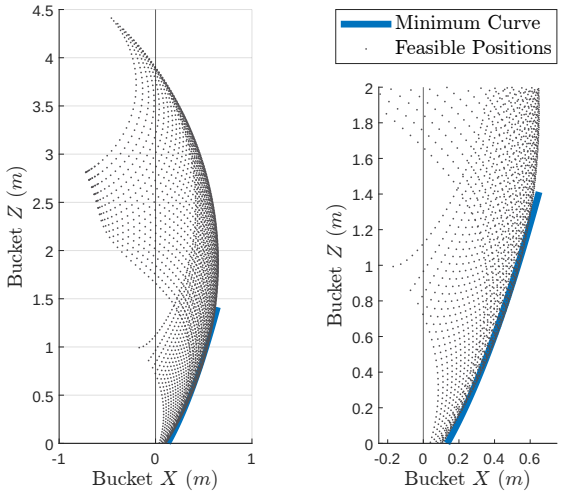

Figure 3.2: Bucket tip feasible positions

against both the vehicle motion and cylinder motion can be found. The electric motors must first be big enough to produce the maximum required power for the drivetrain and hydraulic circuit. The motor flux strength Φ, number of poles P_p, inductances L_q, L_d, and winding resistance R_s are set to reasonable values for a motor to meet the power requirement. From here, the electric motor operating points depend on the gear ratios in the drivetrain and fixed gear in the hydraulic circuit. The motor mechanical output limits can be approximated from electrical inputs:

$$T_{em} = \frac{3P_p\Phi}{2} I_q \tag{3.13}$$

$$\omega_{em} = \frac{1}{L_q P_p} \frac{V_q}{I_q} \tag{3.14}$$

with constraints on motor speed, current, and voltage

$$\omega_{em} \leq \frac{1}{P_p\Phi} V_{max} \tag{3.15}$$

$$0 \leq I_q \leq I_{max} \tag{3.16}$$

$$0 \leq V_q \leq V_{max} \tag{3.17}$$

The motor speed and torque limits depend on the voltage and current provided by the battery. The actual battery is a set of battery packs stacked in series and parallel

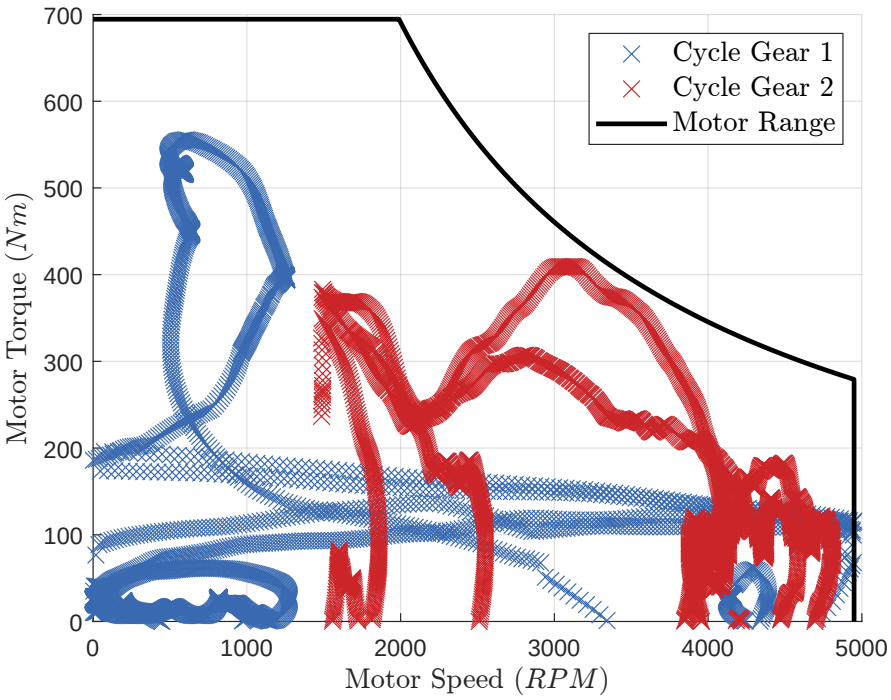

Figure 3.3: Drive motor operating range with example cycle points

to produce the final output current and voltage, plus contributing their energy storage to the total battery energy. For the sake of this work, the battery model will have an output voltage V_{nom} (assumed constant), maximum current $I_{b,max}$, resistance R_b, and nominal energy capacity E_{nom} set to align with industrially available battery packs.

Finally, the gear ratios need to be chosen. The drivetrain transmission has two speeds: one primarily for loading, one for transport. The gear ratio during loading can be set to allow the drive motor to meet the maximum load demand from pile forces. The second gear ratio is set to push all the cycle speeds into the motor's operating range. Fig. 3.3 shows the results of the drive cycle operating points mapped onto the drive motor range.

The electric motor for the hydraulic circuit can be sized similarly, although there is only one fixed gear ratio to select. The gear ratio in this case is applied to allow the electric motor to produce sufficient torque for the main pump without drawing excessive power. The main pump is designed to operate from engine power, which is typically high torque and low speed – the opposite of where the electric motor is most efficient.

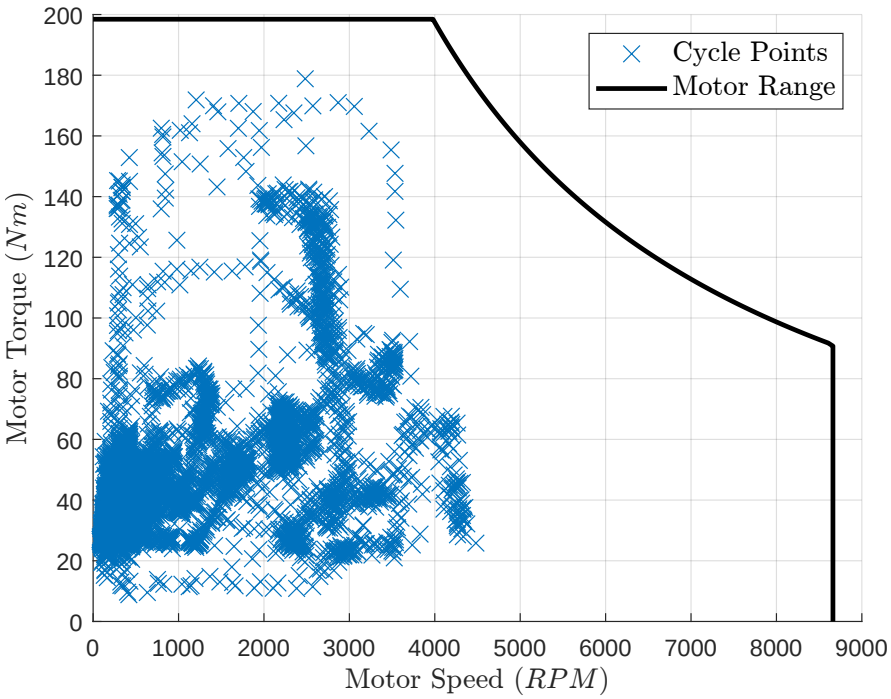

Figure 3.4: Hydraulic motor operating range with example cycle points

Fig. 3.4 shows the results of the pump operating points mapped onto the hydraulic motor range.

The full set of electric component parameters specifications can be found in Appendix A.1.

3.2.2 Cycle Definition

A typical short loading cycle for the target wheel loader is the optimization problem. This cycle is very similar to the one developed in Chapter 2.2.3: The wheel loader travels from the dump site to the material pile, fills the bucket, and travels back to the dump site while lifting the bucket in preparation to unload. The stage and phase breakdown is the same as the diesel version, described in Table 3.1 and shown in Fig. 3.5.

This cycle is not identical to the one used in the previous chapter – the digging and dumping locations have moved to better align with the data available for the target loader, and the bucket load and lifting height is smaller for the compact loader. The diesel formulation will be re-solved with this cycle for comparison between the two

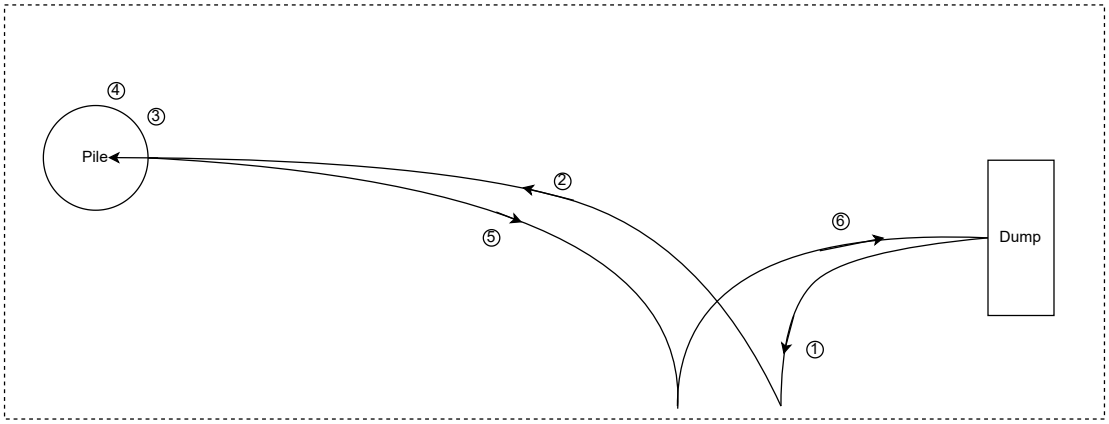

Figure 3.5: Short (V-shape) loading cycle

Table 3.1: Short cycle phase and stage breakdown

Phase	Stage
Transport 1	1. Reverse 1 2. Forward 1
Bucket Loading	3. Digging 4. Stationary Digging
Transport 2	5. Reverse 2 (lifting) 6. Forward 2 (lifting)

powertrains.

3.2.3 Objective Function and Problem Definition

The optimization problem is multi-objective, since both productivity and energy efficiency are desirable. Minimizing cycle time, with a full bucket load carried during each cycle, will encourage productivity. Total battery energy consumed per cycle should also be minimized. The weights $w_1 + w_2 = 1$ determine the balance of emphasis between these costs. Each is normalized by T_{norm} and E_{norm}, which are set to the time and engine shaft output energy from the diesel optimal result. Engine shaft energy is more useful than fuel input energy, since the low efficiency of the engine relative to the battery will make it's input energy drastically higher and the weights in that case would need to always heavily lean towards energy emphasis. The multi-stage optimal control problem

formulation at a high level is the same as the diesel problem except for the cost term representing energy:

$$\min_{x^{(s)},u^{(s)},t_f^{(s)}} \quad J = \sum_{s=1}^{6} w_1 \frac{t_f^{(s)}}{T_{norm}} + w_2 \frac{E_{bat}^{(s)}}{E_{norm}} \tag{3.18}$$

$$\text{subject to :} \qquad \dot{x}^{(s)} = f^{(s)}(x^{(s)}, u^{(s)}), \qquad (s = 1, ..., 6) \tag{3.19}$$

$$x_{min}^{(s)} \leq x^{(s)} \leq x_{max}^{(s)}, \qquad (s = 1, ..., 6) \tag{3.20}$$

$$u_{min}^{(s)} \leq u^{(s)} \leq u_{max}^{(s)}, \qquad (s = 1, ..., 6) \tag{3.21}$$

$$h^{(s)}(x^{(s)}, u^{(s)}) \leq 0, \qquad (s = 1, ..., 6) \tag{3.22}$$

$$g^{(s)}(x^{(s)}, u^{(s)}) = 0, \qquad (s = 1, ..., 6) \tag{3.23}$$

$$x^{(s+1)}(t_0^{(s+1)}) = x^{(s)}(t_f^{(s)}), \qquad (s = 1, ..., 5) \tag{3.24}$$

where s is the stage number, the dynamic equations in Eq. 3.19 are described in Section 3.2.1, Eqs. 2.30 and 3.21 are the state and control bounds, Eq. 3.22 are the inequality constraints, Eq. 3.23 are the equality constraints, and Eq. 3.24 links the stages by constraining the initial and final states of adjacent stages to be equal. The final time of each stage is considered as an additional optimization variable. Optimization occurs over the state variables $x^{(s)}$, control variables $u^{(s)}$, and the final time $t_f^{(s)}$ of each stage.

3.2.4 Physical Constraints

The state and control variables are constrained with upper and lower bounds to provide a realistic setting for the optimal control problem with Eqs. 3.20 and 3.21. These bounds represent operating limits for electrical components and data-based limits for everything else. In addition to these direct constraints on state and control variables, the inequality constraints in Eq. 2.32 include limitations on algebraic combinations of states and control detailed below.

The electric motors each have maximum input power depending on the size of the respective motor. The total motor input power is limited by the battery voltage and

maximum discharge current. When charging the battery through regenerative braking, the net motor power must be less than the maximum charging power. In this case, the drive motor torque and therefore power is negative, switching the direction of current. The maximum battery charging current is a function of SOC, and since SOC changes very little during a single cycle, the charging limit can be assumed constant per cycle. Using the charging current over SOC curve from [32], the lower limit on net motor power is set by the cycle SOC. This constraint still allows power regenerated by the drive motor to go directly to the hydraulic motor through the inverter bus without going through the battery, which could allow greater regeneration and avoids losses at the battery. Since there is an inverter to convert between the battery discharge current and motor input current, the total motor input current is also constrained. Finally, the flow availability and the bucket spacial limits on bucket displacement developed in Section 3.2.1 are included as constraints.

$$P_d - P_{d,max} \leq 0 \tag{3.25}$$

$$P_h - P_{h,max} \leq 0 \tag{3.26}$$

$$P_d + P_h - P_{em,max} \leq 0 \tag{3.27}$$

$$P_{regen,max} + P_d + P_h \leq 0 \tag{3.28}$$

$$u_d + u_h - u_{em,max} \leq 0 \tag{3.29}$$

$$Q_{req} - Q_{mp} \leq 0 \tag{3.30}$$

$$z_{b,min} - z_b \leq 0 \tag{3.31}$$

The terminal constraint on bucket position also remains to force the loading phase to finish with the bucket tip on the pile boundary.

$$z_b(t_f^{(4)}) + \frac{2}{5} x_b(t_f^{(4)}) = 0 \tag{3.32}$$

3.2.5 Boundary Constraints

The boundary constraints are initial and final states for each stage that integrate the multi-stage problem and setup the desired cycle from Section 3.2.2. The initial states of each stage after the first must match the final states of the previous stage. The

Table 3.2: State constraints at initial (i) and final (f) boundaries of each stage

State \ Stage	Reverse 1		Forward 1		Digging		Stat. Digging		Reverse 2		Forward 2	
	i	f	i	f	i	f	i	f	i	f	i	f
SOC	0.6	–	–	–	–	–	–	–	–	–	–	–
ω_d	0	0	0	–	–	0	0	0	0	0	0	0
ω_h	100	–	–	–	–	–	–	–	–	–	–	100
x_p	14	–	–	0	0	–	–	–	–	–	–	14
y_p	-4	–	–	0	0	0	0	0	0	–	–	-4
β	0	–	–	π	π	π	π	π	π	–	–	0
δ	0	–	–	0	0	0	0	0	0	–	–	0
ω_s	0	–	–	0	0	0	0	0	0	–	–	0
x_b	–	–	–	–	0	–	–	–	–	–	–	–
z_b	0	0	0	0	0	–	–	–	–	–	–	4
v_b	0	0	0	0	0	–	–	–	–	–	–	0
ω_b	0	0	0	0	0	–	–	0	0	0	0	0
α	π	π	π	π	π	–	–	$\frac{2}{3}\pi$	$\frac{2}{3}\pi$	$\frac{2}{3}\pi$	$\frac{2}{3}\pi$	$\frac{2}{3}\pi$
A_b	0	0	0	0	0	–	–	0.6	0.6	0.6	0.6	0.6

first stage initial condition must match the final condition for the cycle, except that bucket lowering will be ignored. The constraints are summarized in Table 3.2. Any state boundary that is not specified in the table is subject to optimization – the key advantage of the combined multi-stage formulation.

3.3 Results and Discussion

Results from solving the optimal control problem formulated above are discussed in this section. A high-level comparison of the results for the electric and diesel loaders is shown in Table 3.3. The diesel baseline and optimal solutions are based on the same cycle defined in this chapter. The diesel optimal results is obtained using the formulation from Chapter 2 with this new cycle. The diesel results assume a runtime of 8 hours, and the number of cycles completed assumes that the single cycle is representative and can

Table 3.3: Optimization results comparison between electric and diesel vehicles

Solution	Cycle Energy (kJ)	Cycle Time (s)	Cycles	Runtime
Electric Optimal	604	27.6	535	4.1
Electric Matching	598	29.3	541	4.1
Diesel Optimal	2673	29.3	989	8
Diesel Baseline	3861	44	654	8

be repeated consistently. The optimal electric solution was solved for with cost weights of 0.85 on energy consumption and 0.15 on cycle time, with detailed results shown for this cycle. The Electric Matching solution uses the weight variation curve of Fig. 3.6 to predict the optimal energy consumption if cycle time was the same as the optimal diesel trajectory. The electric cycles and runtime are set by the battery's energy capacity of 90 kWh. While automating and optimizing this diesel vehicle can improve productivity by 33.4% and decrease energy consumption by 31%, electrifying the vehicle can match the productivity while reducing energy consumption by 85%, or a further 78% reduction over the optimal diesel case.

The downside of electrifying this system is the lower relative energy density of batteries compared to diesel fuel. This is shown by the reduction in total cycles completed and overall runtime, which is limited by the energy capacity of the battery. Based on the battery size assumed for this study, the electric vehicle needs 1.8 full battery charges to match the total cycles of the optimal autonomous diesel vehicle and 1.2 charges to match the baseline, human-driven case. This indicates that the battery may be swapped out, recharged, or increased in size to compete with a diesel vehicle's total productivity output – but that it is within reach using this automation method.

Fig. 3.6 shows the trade-off between cost function objectives as the weights vary. Reducing cycle time increases productivity, but also requires higher power and thus consumer more energy. One starred point indicates the set of results that will be discussed in greater detail for the rest of this section, which has greater emphasis on energy consumption. The other starred point indicates the predicted energy consumption for the cycle time to match the optimized diesel cycle.

Fig. 3.7 shows the vehicle trajectory for each stage. The boundary constraints dictate the dump and pile locations, but the middle points in each phase are optimized.

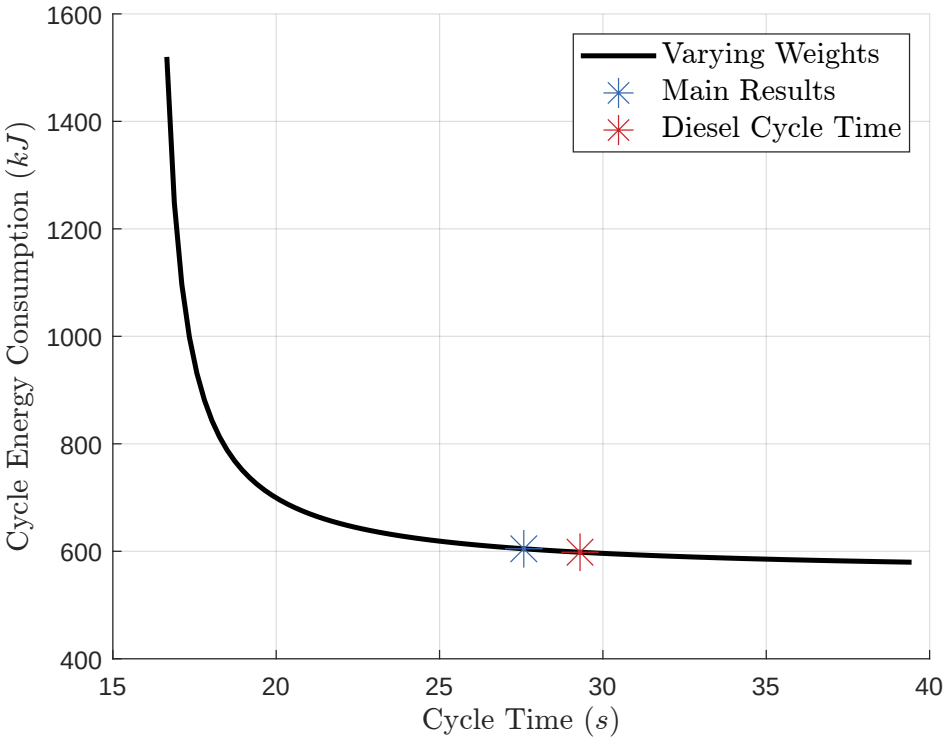

Figure 3.6: Impact of weights on cost function objectives

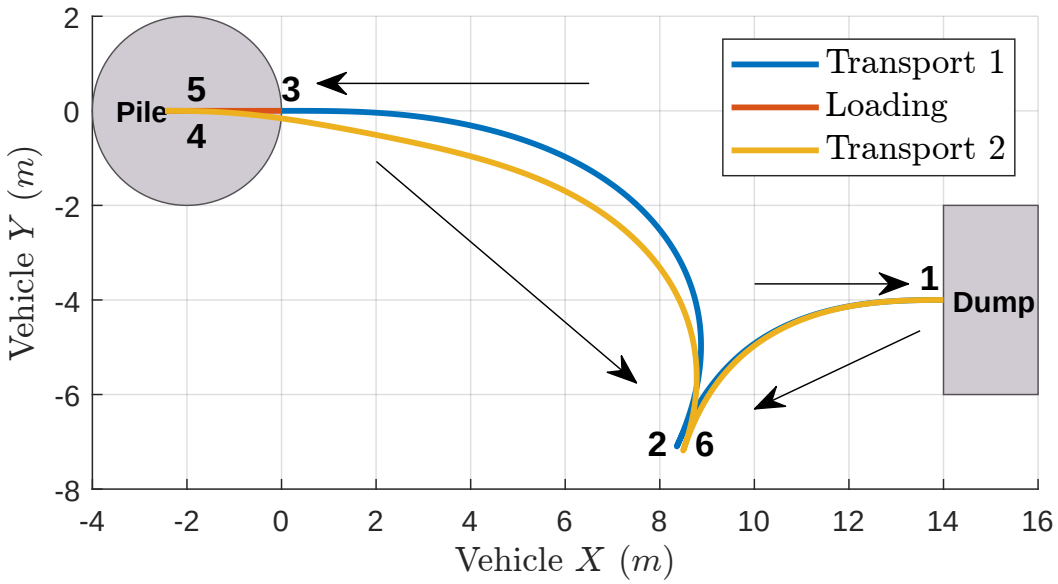

Figure 3.7: Vehicle trajectory

The transport trajectories, especially points 2 and 6, minimize travel distance, which benefits both cycle time and energy consumption. The trajectory for Transport 1 flattens near the end to approach the pile head-on and reach the optimal boundary state to transition into Loading.

Fig. 3.8 shows the trajectory of the bucket tip as a two-dimensional cross-section. In Fig. 3.8a, the pile cross-section is shown and the bucket trajectory includes horizontal vehicle motion. The trajectory avoids large forces on the bucket by cutting near the edge of the pile while filling the necessary area and finishing on the edge of the pile. Fig. 3.8b removes the vehicle motion and shows the isolated bucket trajectory with a map of the feasible positions. Most of the bucket's horizontal depth into the pile comes from driving the vehicle forward, while the bucket itself simply rotates upward to maintain the desired height and cut towards the pile boundary at the end of the loading phase.

Fig. 3.9 shows the operating points of each electric motor on a torque-speed map with lines to mark efficiency. During transport, the drive motor often leaves the high efficiency region to accelerate quickly, driven by the cost on cycle time. Counterintuitively, the drive motor generally runs at lower torques during digging. When sizing

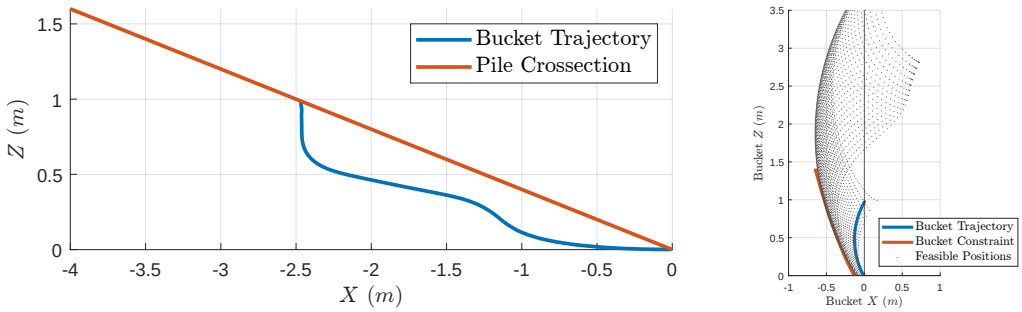

(a) Cross-section including horizontal vehicle motion with pile shape

(b) Isolated from vehicle motion with spacial constraint

Figure 3.8: Bucket trajectory

the motor, the load torque while digging from human driving data was a limiting factor with very high loads. This difference comes from both minimizing the pile forces during digging and coordinating the transition between transport and loading phases, where the vehicle can use the kinetic energy built up in the first transport phase to plunge into the pile, thereby reducing the load that the motor must overcome. For the hydraulic motor, the lifting during transport is done at consistently high efficiency. The digging efficiency is lower and at higher loads than during lifting to complete the most demanding job for the hydraulics. The hydraulic motor does not use its full range of either speed or torque, with the optimal trajectory keeping lifting speed low to limit flow draw rather than running the motor at high speed, suggesting that in the optimized autonomous vehicle this motor could be further downsized with the hydraulic shaft gear adjusted as needed.

Fig. 3.10 shows the power at the input to each motor and the battery. Battery efficiency decreases as a function of motor power – or current – draw, which motivates the motors to operate at relatively low power. During loading, the battery power is kept nearly constant while the motors trade off higher power operating times. During the second transport phase, the hydraulic motor power, driven by lifting speed, is mostly consistent except when the drive motor regenerates power through braking, allowing the lifting to increase.

Fig 3.11 shows the electric motor speeds, vehicle speed, and gear ratio over time. The drive motor speed follows consistent acceleration-deceleration patterns during the

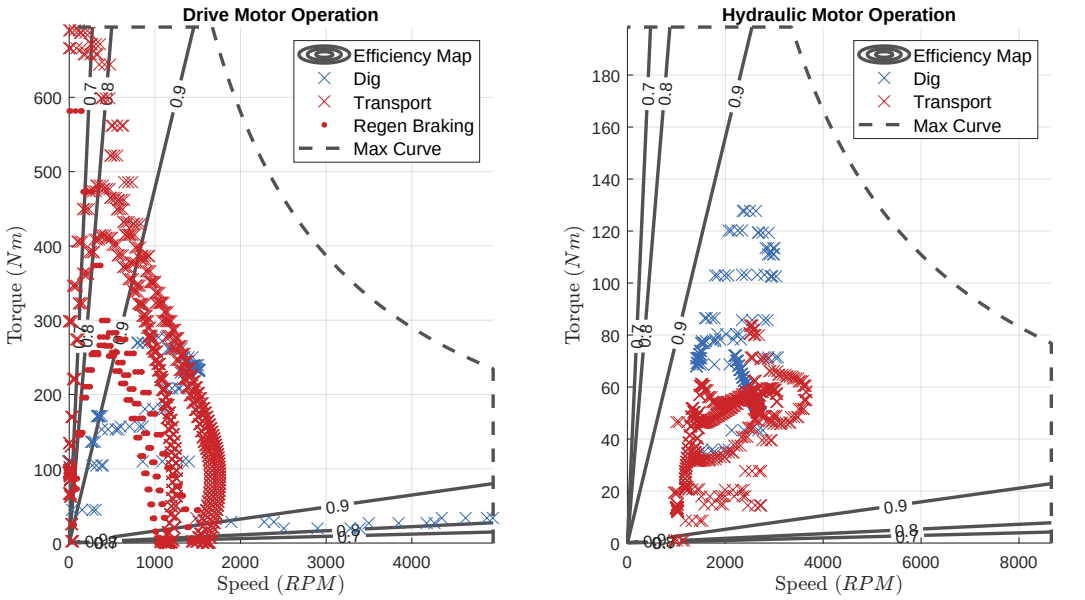

Figure 3.9: Electric motor operating points

transport phases. As the gear ratio changes when entering the loading phase, the motor speed spikes very high while vehicle speed remains constant, then both speeds are quickly pulled down by the load from the pile. During the second transport phase, the vehicle comes to a complete stop between stages while lifting slowly. Each time-series plot in this section has shown that the stationary digging stage (5) has been effectively removed in this optimal solution. The motor speeds during the loading stages show why it is no longer necessary – the drive motor speed drops quickly as the vehicle plunges into the pile, pulled down by the pile load, while the hydraulic motor speed remains higher to ensure enough flow is available for the bucket to complete its motion, dictated by the flow constraint. This, along with lifting while the vehicle speed is low or stopped, is only made possible by separating the powertrain with two electric motors rather than running them on the same shaft as in the diesel-powered vehicle.

3.4 Conclusion

This study used nonlinear programming to formulate and solve a drive cycle optimization problem for an electrified off-highway vehicle modeled on a Compact Wheel Loader.

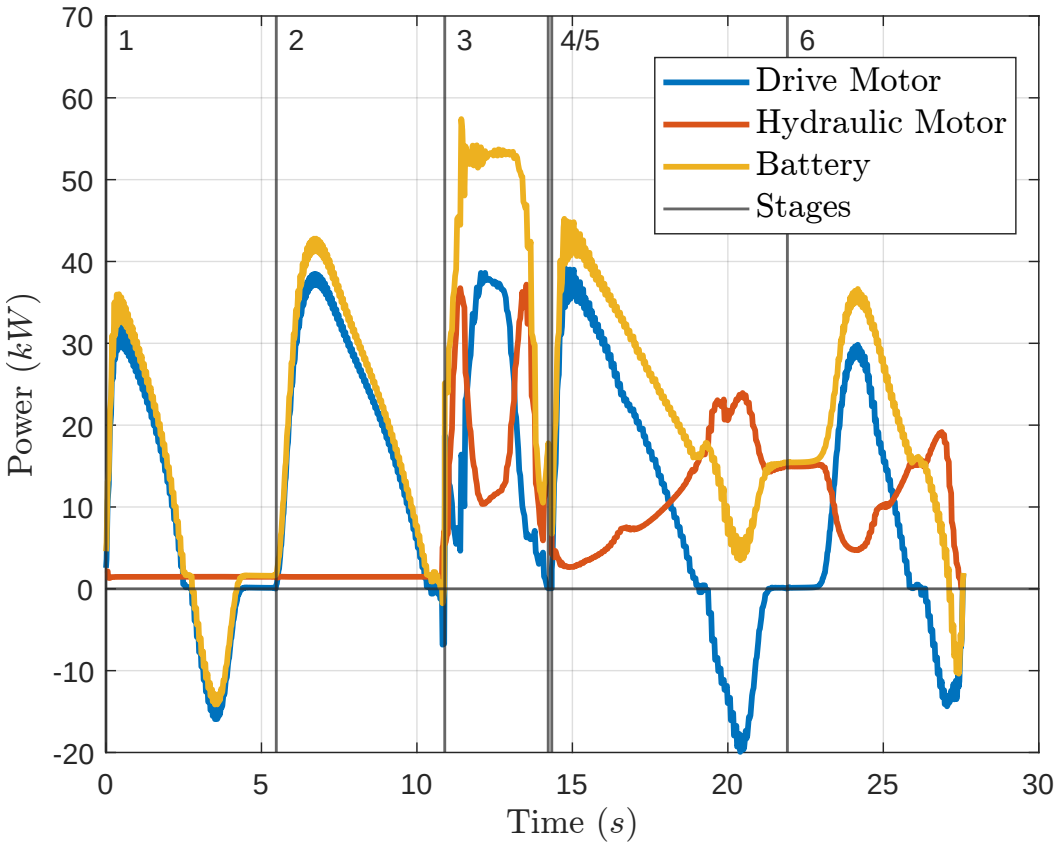

Figure 3.10: Electric motor input power

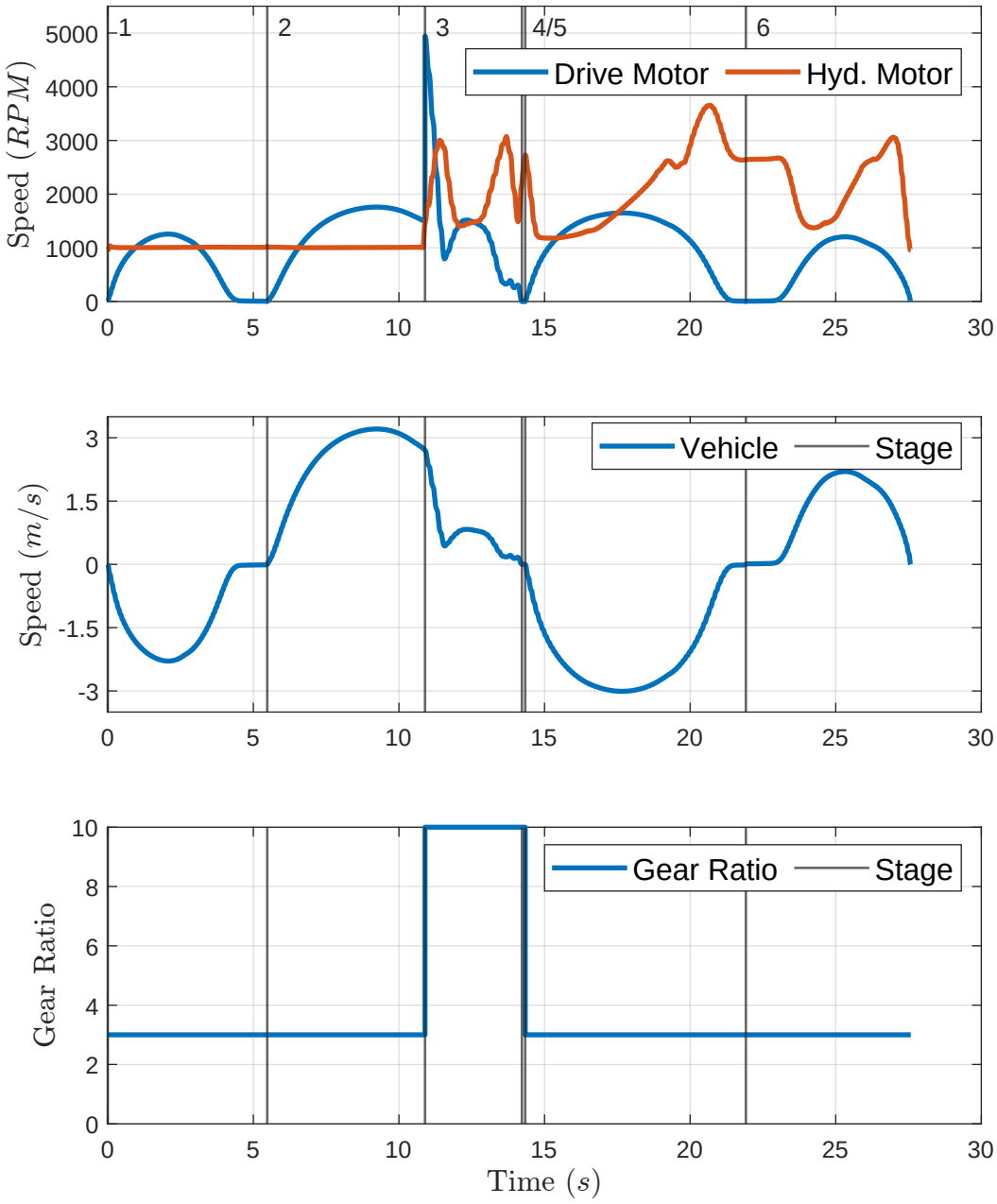

Figure 3.11: Electric motor speeds, vehicle speed, and mode-based gear ratio

The high potential for energy savings via electrification is demonstrated, with the electric vehicle consuming 78% less energy than the optimal autonomous diesel vehicle for the same cycle – although this comparison does not include the efficiency of generating the energy stored in the battery. The overall productivity of a battery-powered autonomous and optimized electric vehicle compared to a sub-optimal human-driven and optimized autonomous diesel vehicle is compared, finding that the electric vehicle requires 1.2 and 1.8 full battery charges to match. This lays out a pathway for the electrification of wheel loaders larger than those found in industry, using automation and optimization to overcome limitations imposed by electric energy density.

The formulation can find the best-case optimal trajectory for a given set of model parameters and drive cycle, with the results representing one cycle typical in literature and an electric loader sized based on a human driven data. This can be used to predict the ranges of potential cycle time and energy consumption for any similar system depending on model parameters and desired cost weight emphasis. A battery-electric architecture with two PMSM motors splitting the powertrain into drive and hydraulic functions is detailed. The objective function used for this study highlights the trade-off between productivity and energy efficiency, which is especially vital when the vehicle is powered by a battery with much lower energy density than diesel fuel. The results also show the significance of well-designed physical and boundary constraints for this problem to maintain a realistic simulation environment with interpretable results. Discussion of the results elucidates why they are optimal within the boundaries of the problem. The results obtained in this study have yet to be validated in simulation on a more robust and accurate dynamic model or experimentally, yet they show significant promise for the potential energy benefit of electrifying, automating, and optimizing wheel loaders. Future work could also incorporate battery aging into the optimization, by changing the cost function, and the hydraulic circuit efficiency's dependence on operating conditions.

Chapter 4

Simulation and Experimental Hardware-in-the-Loop Evaluation of Optimal Results

4.1 Introduction

Results obtained from solving the optimization problem presented in Chapters 2 and 3 need to be validated to ensure that the proposed state trajectories and energy savings are realistic. For verification of the results, a higher order validated model that was unsuitable for use in optimization can run a simulation using the optimal trajectory as a tracking reference. The optimal results are converted to a form that can serve as inputs to the validated model so the capability for the modeled vehicle to follow the proposed trajectory can be assessed. This process provides an effective validation of the optimal results for both the diesel and electric powertrains.

[31, 32] propose and use a Hardware-in-the-Loop (HiL) Testbed with a real engine to demonstrate optimal results for connected and autonomous on-road vehicles. This method is simpler, safer, and less costly than field testing with a full vehicle. Experimental evaluation using a Hardware-in-the-Loop (HiL) system provides additional confidence for the diesel results. The HiL testbed was built with a real wheel loader engine connected to a dynamometer. The dynamometer is controlled in real-time to

provide the engine load determined by the rest of the system model. Collaborators have developed a control system to operate the HiL testbed and performed the experiment [47] using results from solving the optimal formulation developed in the previous chapters. The formulation from Chapter 2.2.1 is applied to the cycle in Chapter 3.2.2 for a Compact Wheel Loader. A light-duty cycle is used with a constraint added to limit the engine torque and load within bounds that are safe for the lab. The fuel consumption is measured directly from the engine. This combination of the validated model with a real engine will give highly accurate results to validate the output of the optimal solution. While the results for the electrified wheel loader will not be evaluated experimentally in this way, the simulation of the validated model can be compared to the HiL Testbed for the combustion engine powertrain to determine the level of confidence in the simulation, which can then be extended to the electrified powertrain.

A version of the high-order diesel system model used in this chapter was first presented in [46] for a similar vehicle. The HiL evaluation of optimal results for the Compact Diesel Wheel Loader were originally presented in [47] with comparison to a baseline cycle.

4.2 Methods

4.2.1 High-Order Diesel Model

Fig. 4.1 shows an overview of the high-order validated diesel system model used in this section. Key differences from the control-oriented model used in Chapter 2 include the engine, torque converter, transmission shift schedule, hydraulic main pump, priority valve, hydraulic work circuit, and hydraulic steering circuit.

Engine

The engine shaft dynamics are given by

$$\dot{\omega}_e = \frac{1}{J_e}(T_e - T_{tc_p} - T_{mp} - T_{bp)} \tag{4.1}$$

where J_e is the lumped engine shaft inertia, ω_e is the engine speed, and T_e, T_{tc_p}, T_{mp}, T_{bp} are the engine torque, torque converter load, main hydraulic pump load, and brake

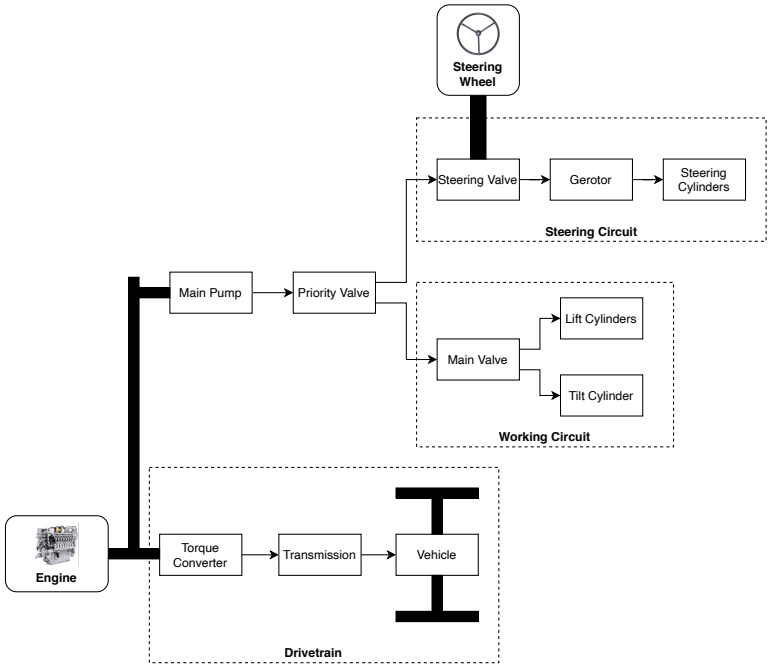

Figure 4.1: Diesel system schematic

pump load. Based on field testing data, the brake pump torque can be approximately constant.

The engine torque and fuel rate are modeled by a static engine map lookup table, with inputs of throttle and speed and outputs torque and fuel rate. The mapping is calibrated on the engine using the HiL setup in Section 4.2.4.

Drivetrain

The primary differences between the drivetrain model presented here and the one in Chapter 2 are the torque converter model and the transmission using the actual shift schedule along with gearshift dynamics. The shaft dynamics, loads, and algebraic conversions are the same.

The torque converter does not have a lock-up clutch and is modeled using a lookup table with the speed ratio, torque ratio, and the K-factor as defined by the following

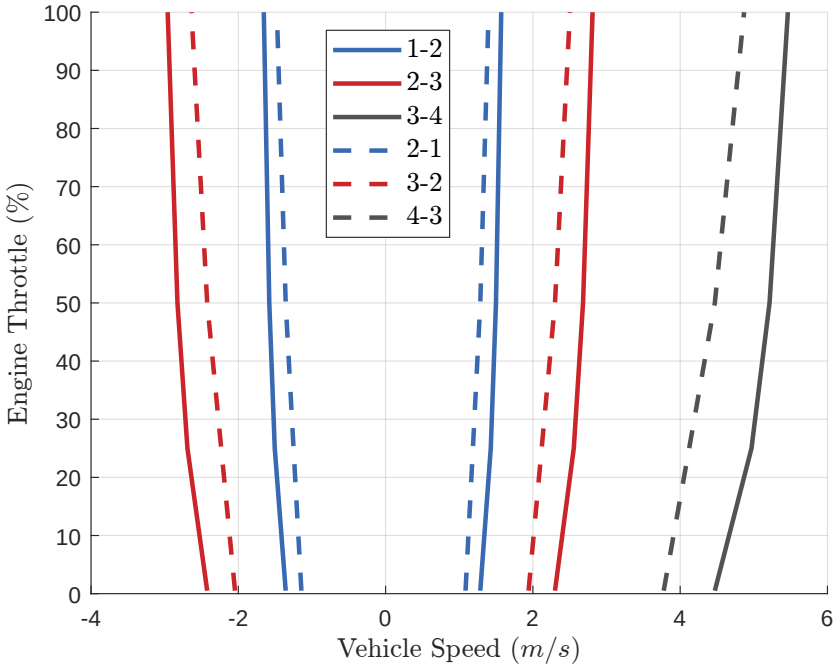

Figure 4.2: Automatic transmission shift schedule

equations [48]:

$$speed\ ratio = \frac{\gamma \omega_d}{\omega_e} \tag{4.2}$$

$$torque\ ratio = \frac{T_d}{\gamma T_{tc_p}} \tag{4.3}$$

$$K - factor = \frac{\omega_e}{\sqrt{T_d/\gamma}} \tag{4.4}$$

where ω_d is the driveshaft speed, T_d is the driveshaft torque, and γ is the transmission gear ratio. The speed ratio of a torque converter uniquely determines the torque ratio and the K-factor, which then give the torques. The torque converter connects to the gearbox.

The modeled wheel loader uses an automatic 4-speed transmission. Gearshifts are determined by a shift schedule, shown in Fig. 4.2, where vehicle speed and engine throttle determine any change in the commanded gear that corresponds to values for γ. Since the shift dynamics are fast relative to the rest of the drivetrain dynamics and shift

transience has negligible effect on energy consumption, the gear shifts are approximated by a first order delay with a time constant of 0.5 seconds. The dynamics at the final drive shaft are given by

$$J_d\dot{\omega}_d = T_d - T_{rr} - T_{pile} - T_b \tag{4.5}$$

where J_d is the lumped inertia of the driveshaft, ω_d is the driveshaft speed, and T_{rr}, T_{pile}, T_b are the rolling resistance torque, pile resistance torque, and brake torque. The shaft friction has been neglected because it is negligible compared to the load torques. The driveshaft loads can be calculated by the following:

$$T_{rr} = \frac{R_w}{k_f}\mu mg \tag{4.6}$$

$$T_{pile} = \frac{R_w}{k_f}F_h \tag{4.7}$$

where R_w is the wheel radius, k_f is the final drive ratio, μ is the rolling friction coefficient of the wheels, m is the total vehicle mass, g is the acceleration due to gravity, and F_r is the pile resistance force. The brake torque applied to the final drive shaft is modeled as linearly related to the brake pedal command. Due to the low vehicle speeds, the aerodynamic losses can be neglected. The vehicle speed can then be calculated by

$$v = \frac{R_w}{k_f}\omega_d \tag{4.8}$$

Hydraulic Circuit

The hydraulic circuit, including the main pump, priority valve, work circuit, and steering circuit have been developed by collaborators Zhao et. al. and Yu et. al. detailed in [46, 49]. This is a 22nd-order model of the pressure, flow, and cylinder dynamics in the system. Including these dynamics ensures that the energy losses of the hydraulic system and its capability to track the desired optimal trajectory will be validated. In Chapter 2, this system was simplified into an energy balance with constant efficiency to convert power at the bucket to power at the engine shaft.

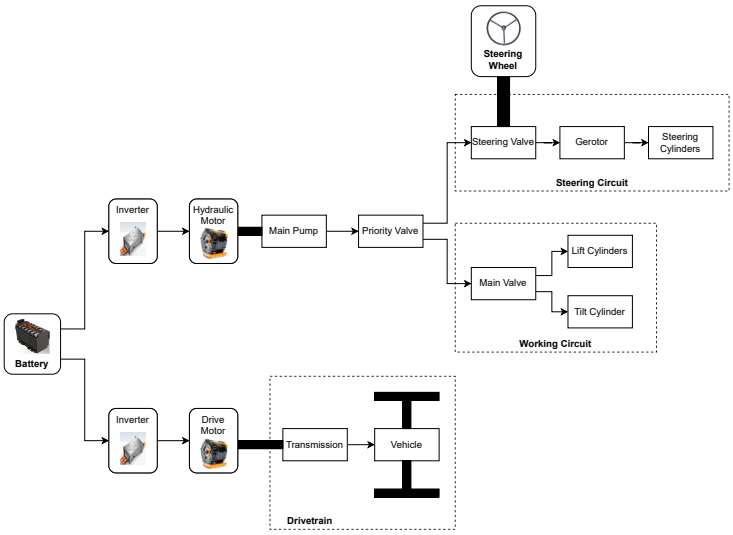

Figure 4.3: Electric system schematic

Steering

The output of the hydraulic steering circuit is steering angle δ. From here, the same bicycle model vehicle dynamics from Section 2.2.1 are used to obtain position and heading angle by coupling with vehicle speed:

$$\dot{x}_p = v \cos \beta \tag{4.9}$$

$$\dot{y}_p = v \sin \beta \tag{4.10}$$

$$\dot{\beta} = \frac{2}{L} v \tan \frac{\delta}{2} \tag{4.11}$$

4.2.2 High-Order Electric Model

Fig. 4.3 shows an overview of the high-order electric system model used in this section. Key differences from the control-oriented model used in Chapter 3 include the electric motors, transmission, and hydraulic circuit. The hydraulic circuit model and vehicle dynamics are the same as in the diesel version above, with the hydraulic main pump powered by an electric motor through a fixed gear.

Battery

As in Chapter 3, the battery is a voltage source with a resistance model for loss, and the SOC dynamic matches discharge power to net motor power with the assumption that inverters can convert voltage and current at the battery and motor as necessary:

$$\dot{SOC} = -\frac{V_{bat} - \sqrt{V_{bat}^2 - 4R_{bat}P_{em}}}{2R_{bat}} \tag{4.12}$$

where SOC is the battery state of charge, V_{bat} is the constant battery voltage, R_{bat} is the battery resistance, and P_{em} is the net electric motor power. Motor power with loss for $i = d, h$ is given by:

$$P_{em} = T_d\omega_d + loss_d + T_h\omega_h + loss_h \tag{4.13}$$

$$loss_i = P_{max,i}\left(p_1\frac{T_i}{T_{max,i}}^2 + p_2\frac{\omega_i}{\omega_{max,i}}^2 + p_3\frac{T_i}{T_{max,i}}\frac{\omega_i}{\omega_{max,i}} + p_4\right) \tag{4.14}$$

Electric Motors

While motor dynamics in Chapter 3 only considered mechanical torque and speed, the electrical dynamics are included here using the Park transform D-Q model [50]:

$$\dot{I}_{i,d} = \frac{1}{L_{i,d}}(v_{i,d} + L_{i,q}P_p\omega_i I_{i,q} - R_i I_{i,d}) \tag{4.15}$$

$$\dot{I}_{i,q} = \frac{1}{L_{i,q}}(v_{i,q} - L_{i,d}P_p\omega_i I_{i,d} - R_i I_{i,q} - \Phi P_p\omega_i) \tag{4.16}$$

$$\dot{\omega}_i = \frac{1}{J_i}(T_i - T_{i,load} - b_m\omega_i) \tag{4.17}$$

$$T_i = \frac{3}{2}P_p\Phi I_{i,q} + \frac{3}{2}P_p(L_{i,d} - L_{i,q})I_{i,d}I_{i,q} \tag{4.18}$$

where the subscripts i, d, q represent the respective motor, d-axis, and q-axis, I, V, ω_m are axial current, axial voltage, and output speed, and P_p, Φ, R, L, b, J_m are the number of poles, magnetic flux strength, resistance, inductance, friction coefficient, and lumped motor inertia. The drive motor inertia J_d includes the vehicle inertia and is dynamic

during gear shifts. The load on each motor is given by:

$$T_{d,load} = \frac{1}{\gamma}(T_{rr} + T_{pile} + T_b) \tag{4.19}$$

$$T_{h,load} = \frac{1}{\gamma_h} T_{mp} \tag{4.20}$$

where γ_h is the fixed gear ratio between the electric motor and the hydraulic main pump.

Drivetrain

The electrified drivetrain uses a two-speed, mode-based transmission with one gear ratio for transport and one for loading. The dynamics are modeled with a first-order delay similarly to the engine model, but the shift schedule is replaced by simply shifting gears at the phase transition boundary.

4.2.3 Autonomous Vehicle Simulation

Cycle Creation

To evaluate the optimal trajectory in a simulation of the autonomous vehicle, the results must be converted to references to track and external forces to apply. All inputs are filtered and resampled to ensure smooth signals. The necessary simulation inputs are summarized below:

- Engine speed (diesel only)
- Hydraulic e-motor speed (electric only)
- Vehicle speed
- Vehicle X-Y position
- Horizontal pile force
- Lift and tilt cylinder speeds
- Lift and tilt cylinder forces

The engine speed, hydraulic e-motor speed, vehicle speed, and vehicle X-Y position are taken directly from their respective states in the optimal solution. The vehicle position is also split by stage for the position tracking algorithm.

The horizontal pile force, along with bucket tip forces, can be found using the same

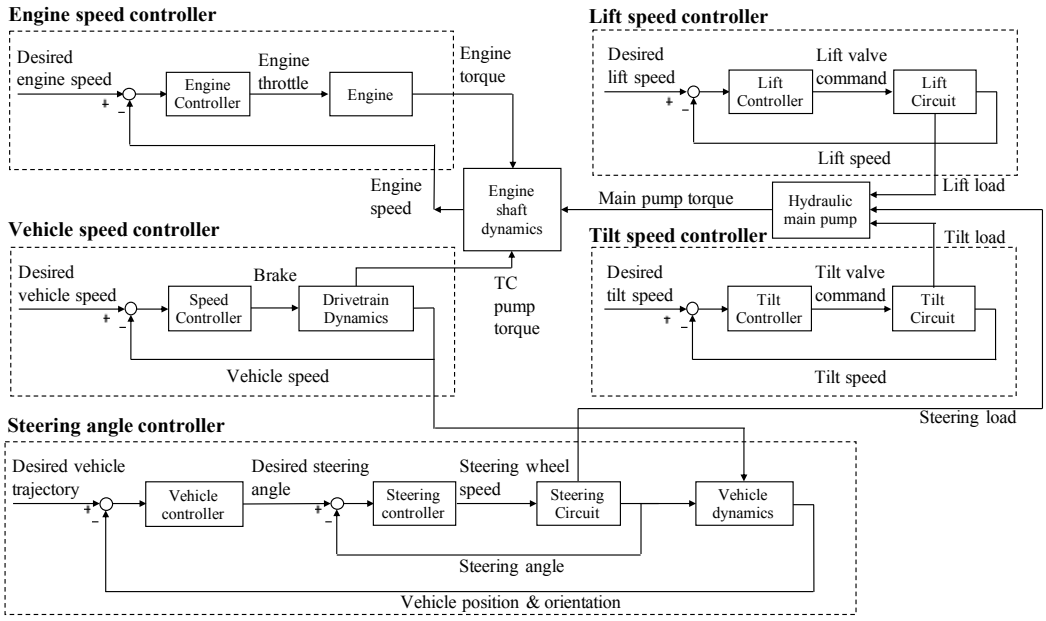

Figure 4.4: Diesel autonomous vehicle control system

FEE model from Chapter 2.2.1. The lift and tilt cylinder speeds and forces are found using a Lagrangian model of the bucket linkage mechanism, converting bucket motion and forces from the optimal results to cylinder motion and forces. The force and linkage models are developed by Yu et. al. in [37].

Diesel Control Architecture

To simulate the performance of an autonomous vehicle for the tracking problem formulated above, an architecture for the low-level control is needed. The model described in Section 4.2.1 is a high-order strongly nonlinear system with states coupled to form a challenging Multi-Input Multi-Output (MIMO) system. For this vehicle, the engine speed is a key variable to propagate the necessary power to both the drivetrain and the working circuit. Based on this physical insight, a novel control architecture is proposed in this section to decouple the MIMO system to several Single-Input Single-Output (SISO) systems in Fig. 4.4.

Five independent controllers are designed for each subsystem of the wheel loader to track its corresponding reference. The vehicle speed controller propels the drivetrain

dynamics to reach the desired vehicle speed. The steering controller forces the vehicle dynamics to follow the desired trajectory. The lift controller and tilt controller work together to make the bucket follow the desired profile. Although the model has been decoupled, the fundamental structure of the wheel loader of Figure 1 has been maintained since all subsystems demand the power from the engine through the engine shaft dynamic equation. The references are generated from the optimal cycle as described above for high level trajectory planning, where the optimized engine speed is vital not only for energy efficiency, but also for the tracking performance for the entire trajectory.

The steering control section uses a two-loop structure. The outer loop computes the necessary steering angle to track the vehicle position and the inner (actuator) loop controls the steering wheel to produce this desired steering angle through the hydraulic circuit dynamics. The outer loop uses a pure pursuit path tracking strategy [51, 52] which determines the steering angle by looking ahead along the reference path and turning towards a future point. The lookahead distance depends on velocity, and must be tuned to avoid cutting corners and reduce oscillations.

Electric Control Architecture

The electrified system architecture naturally decouples the control for the drivetrain and hydraulic systems, as they are now driven by separate electric motors. Similarly to the diesel system after the engine shaft dynamics are handled, there are five independent controllers that can be treated as SISO systems. With the powertrain decoupled, the desired drive motor speed is determined by vehicle speed and transmission gear ratio, while the desired hydraulic motor speed is a direct output of the optimization solution. While the hydraulic cylinder and steering control loops can be kept from the diesel control system above, the remaining challenge is designing the two electric motor controllers.

The PMSMs use vector control with feedforward cancellation, which creates linear feedback systems – similar to a DC motor – with good dynamic performance, derived in [53]. Fig. 4.5 gives an overview of the motor control architecture. The control system has two loops: speed control and current control. Speed control is the outer loop to track the main objective, which determines the necessary torque. The inner loop produces this torque with D- and Q-axis voltages as the control variables. Examining

Eq. 4.18 shows that the output motor torque is nonlinear. Note that since $L_q > L_d$, any D-axis current will reduce the generated torque. By maintaining I_d at 0, the torque will be proportional to I_q, giving tracking references for the inner current control loops. Examining Eqs. 4.15 and 4.16 shows that the current dynamics are also nonlinearly coupled. Using a feedforward voltage that depends dynamically on speed and current to cancel the coupling terms reduces the current equations to linear dynamics to determine the control voltage:

$$\dot{I}_{i,d} = \frac{1}{L_d} v^*_{i,d} - \frac{R_s}{L_d} I_{i,d} \tag{4.21}$$

$$\dot{I}_{i,q} = \frac{1}{L_q} v^*_{i,q} - \frac{R_s}{L_q} I_{i,q} \tag{4.22}$$

where the actual voltages are a combination of the control voltage and the feedforward cancellation:

$$v_{i,d} = v^*_{i,d} - L_{i,q} P_p \omega_i I_{i,q} \tag{4.23}$$

$$v_{i,q} = v^*_{i,q} - L_{i,d} P_p \omega_i I_{i,d} + \Phi P_p \omega_i \tag{4.24}$$

For this controller to be effective, it must be assumed that the motor model parameters are estimated accurately and the axial currents can be measured or estimated.

The drive motor speed control has an additional input to consider with braking. When the vehicle is accelerating or coasting, the torque is positive and will be produced by current control as expected. However, when the vehicle is decelerating, the torque from the speed control loop will be negative, and must be produced by a combination of negative current (regeneration) and mechanical braking. To maximize energy efficiency, the controller prioritizes using regenerative braking via negative current as much as possible. The battery SOC limits its recharge current, which constrains the power that the motor can send back as described by the regeneration constraint in Chapter 3.2.4. The negative motor current saturates at this power limit, and the rest of the speed control must be fulfilled with mechanical braking.

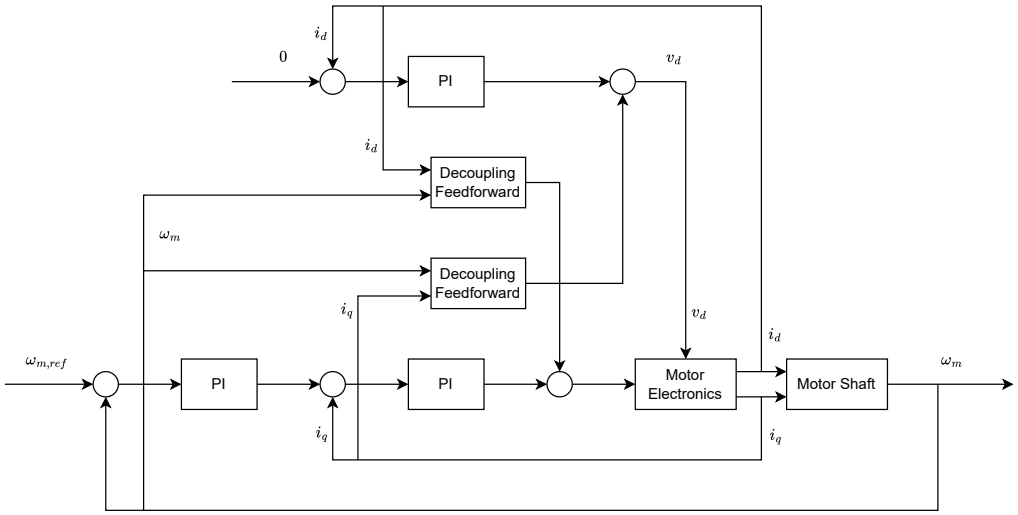

Figure 4.5: Electric motor control system

4.2.4 Hardware-in-the-Loop Experiment

A Hardware-in-the-Loop (HiL) experiment provides an additional level of evaluation and validation for the optimized results from the diesel vehicle. It is clear that the engine efficiency is the most impactful part of reducing fuel consumption for the diesel powertrain. The engine map used in the simulation is limited to static calibration, while the engine's operating point in the optimized cycle is highly dynamic. Using a real engine loaded by a hydro-static dynamometer provides additional confidence in the evaluation of the results without the time investment or safety limitations of a fully autonomous vehicle. The engine can be controlled to track a speed reference while the dynamometer is controlled to apply a dynamic load. The system design, setup, control, and experiment was performed by collaborators and is described in [47]. The HiL results use the optimized engine speed and load, and are included in the results section below.

4.3 Results and Discussion

This section presents the results of simulations of an optimal cycle trajectory for both diesel- and electric-powered vehicles, with HiL experiment included for the diesel vehicle. The HiL experimental results are for engine speed and torque, with the engine load

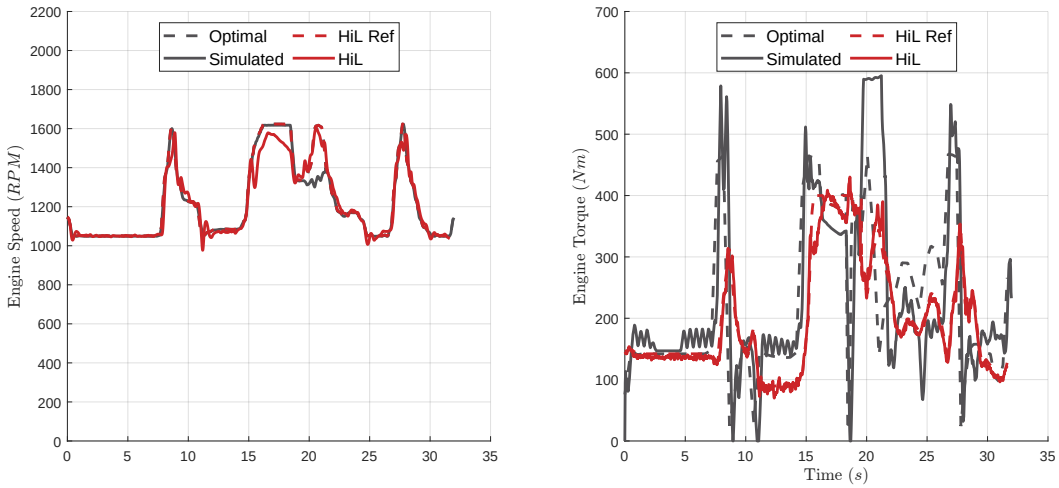

Figure 4.6: Diesel simulation tracking performance of engine

predicted by the optimization results applied as the load on the real engine.

4.3.1 Tracking Performance

Fig. 4.6 compares the simulated engine speed and torque to the optimal trajectory. The engine throttle is used as the control variable to track speed, while torque responds with throttle to the load generated by the rest of the model to maintain desired speed. The simulation shows that the engine speed is mostly tracked well with exceptions during the loading phase and beginning of second transport phase with lifting. For the simulation, engine speed can be followed during loading but does no increase at the beginning of the second transport phase. The tracking error occurs because the total engine load is too high, which is shown by the engine torque reaching its maximum value at this time. For the HiL experiment it is the reverse – loading phase speed has a small error while the transport phases are not an issue. The small errors in engine speed during for the HiL system come during peak power operation, the loading phase, since controlling the system at the peak of its performance envelope is difficult. and that the engine torque is close to the prediction from the optimal solution.

Fig. 4.7 shows the tracking performance in the diesel system of the drivetrain and hydraulic subsystem outputs: vehicle velocity and lift and tilt cylinder velocities. The vehicle velocity on the left demonstrates that the drivetrain is mostly able to maintain

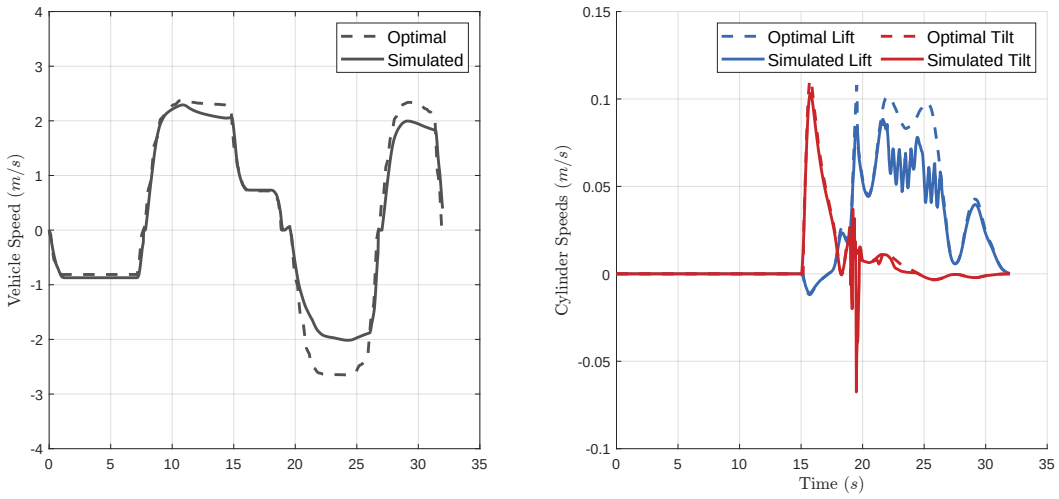

Figure 4.7: Diesel simulation tracking performance of vehicle and cylinder speeds

the desired speed, although the simulated result during the second transport phase does not able to reach the optimal peak. The worst error comes during the first half of this phase, when he engine speed also had an error. If the optimization under-predicts the load on the engine from the hydraulic system while running at high torque, the engine will be unable to compensate further. Since the drivetrain and hydraulics are connected to the same shaft, an issue from the hydraulic system impacts the drivetrain and thus vehicle speed. The lift cylinder velocity is trends close to the optimal trajectory, but is a too low for the first half of lifting. This is an issue with the flow available from the main pump, which limits the achievable cylinder speeds. The optimal cycle would need to incorporate the flow-based relationship between engine speed and potential cylinder motion and either increase desired engine speed or decrease desired lift velocity in order to improve the simulated tracking. With insufficient flow available for the cylinders, the main pump torque will increase and impact the engine and drivetrain performance. The tilt cylinder velocity tracks well. Its main operation is during the loading phase, where the engine runs at higher speed and power than transport, so flow availability is not an issue.

Fig. 4.8 shows the speed tracking and torque comparison for both electric motors. In the simulation, voltage is controlled to produce torque and track speed. Both motors are able to follow the optimal speed trajectories closely. The motor torque is also close

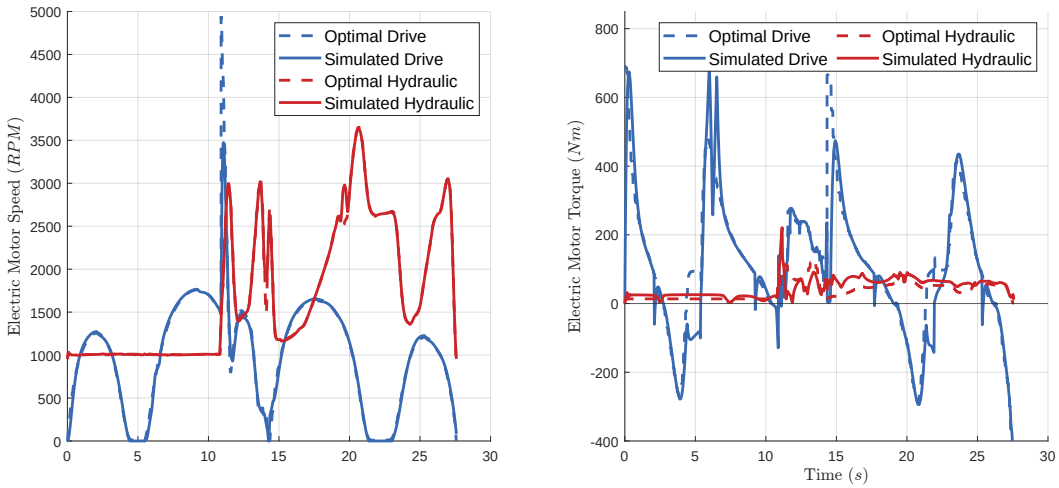

Figure 4.8: Electric simulation tracking performance of motors

to the prediction from the optimal cycle, especially for the higher powered drive motor, which consumes most of the energy for the system. This validates the motor dynamics and that the optimization is constrained appropriately for these motor sizes.

Fig. 4.9 shows the tracking performance in the electric system for the drivetrain and hydraulic outputs. The vehicle velocity is followed very well, which is directly related to drive motor speed through only a transmission gear ratio. This shows that ignoring the gear shifting dynamics in the optimization do not prevent the system from following the desired trajectory with this mode-based transmission. The cylinder speeds also closely track the optimal trajectory. Using the flow constraint in the optimal formulation ensures that the pump speed is high enough to provide adequate flow for the cylinder motion and steering – a similar constraint would be useful for the diesel formulation. Considering steering flow in the formulation is necessary since it has priority over the work circuit, meaning if the available flow were not sufficient for both systems, the work cylinder tracking performance would suffer.

The electrified simulation results highlight a key advantage this system has over the diesel vehicle. By splitting the powertrain onto two separate motors, in addition to allowing more efficient operation, it is much easier to design a control system and to follow the desired optimal trajectory.

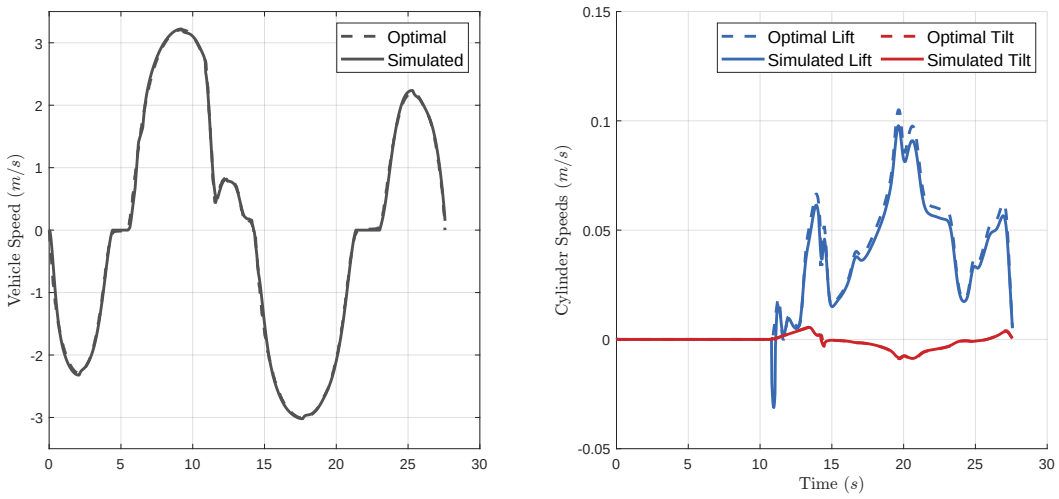

Figure 4.9: Electric simulation tracking performance of vehicle and cylinder speeds

4.3.2 Energy Analysis

Table 4.1 compares the energy consumption predicted by the optimized trajectory to the simulation and HiL evaluation of the diesel vehicle and simulation of the electric vehicle. For the diesel vehicle, the simulation is within 2.8% and the HiL within 0.7% of the optimal prediction, which validates the accuracy of predictions from the optimization's control-oriented model. Simulation of the electric vehicle shows 6.0% higher energy consumed than predicted by the optimal trajectory. While the electric system had better tracking performance in the simulation than the diesel system, the percent energy difference is higher. During optimization, neither system includes the steering subsystem when predicting the energy or fuel consumption. Since the electric system has much lower consumption, the steering energy is a higher portion of the total energy. The difference between energy in the electric simulation and optimal results is 36.3 kJ, with a difference 36.1 kJ in hydraulic motor output energy. The input to the steering system is 40.4 kJ, while the simulated work circuit consumes slightly less energy than predicted.

There are two key outcomes of optimizing the cycle trajectory for energy efficiency: work done is minimized while meeting cycle requirements, and the powertrain operating point is optimized for total efficiency. Since the optimization formulation is multi-objective to also minimize cycle time, some efficiency is sacrificed for speed according

Table 4.1: Energy consumption results of simulations and HiL experiment compared to optimal predictions

Solution	Optimal Energy (kJ)	Simulated Energy (kJ)	Energy Difference (%)
Diesel Simulation	2694	2770	2.8
Diesel HiL	2694	2676	0.7
Electric Simulation	605	641	6.0

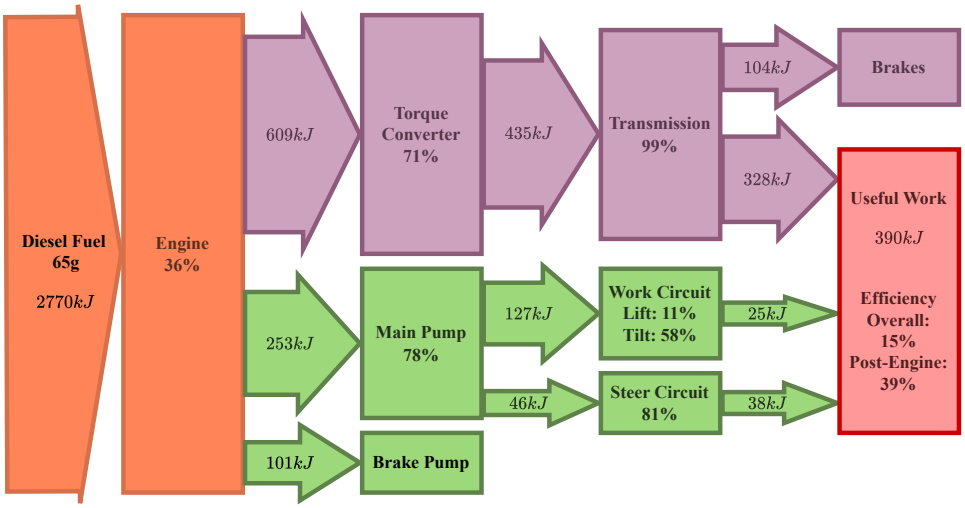

Figure 4.10: Diesel vehicle energy flow from the simulation with average efficiencies and total energy consumption.

to the cost weights. Figs. 4.10 and 4.11 show energy flow diagrams for the diesel and electric vehicles using results from the simulations. The final work output produced by each system is very similar since they must complete the same cycle, with the electric vehicle work actually slightly higher mainly due to its better tracking performance. The difference between the two systems comes from optimization of the powertrain rather than work output.

The major efficiency advantage of electric power is immediately obvious looking at the efficiency of each power source: the diesel engine averages 36%, while the battery is 94%. This accounts for most of the electrification gains. The electric vehicle also eliminates wasted braking energy, reducing drivetrain power and relying on regenerative braking. The architecture of the electrified system accounts for the remaining

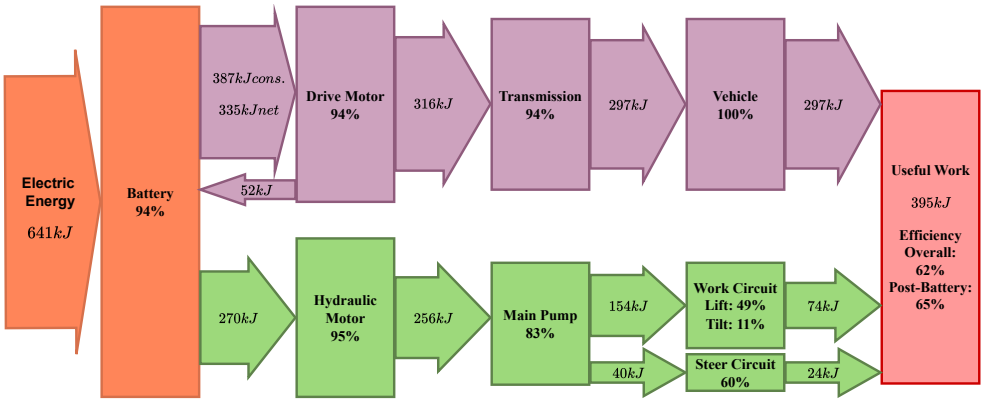

Figure 4.11: Electric vehicle energy flow from the simulation with average efficiencies and total energy consumption.

improvement. Removing the torque converter, which averages 71% efficiency in the diesel system, further reduces the drivetrain energy consumption. Splitting the drivetrain and hydraulic system onto separate motor shafts leads to an increase in main pump efficiency, from 78% to 83%, since the hydraulic motor speed is chosen solely for the pump. The diesel system has an overall efficiency of 15%, while the electric system is 62%. Much of this improvement comes from replacing the engine; however, even when discounting the power source efficiency the electric system is much better: diesel system efficiency of 39% is increased in by electrification to 65%.

4.4 Conclusion

This chapter shows the validation and evaluation of optimal cycles for diesel and electric wheel loaders. The diesel system is evaluated both in simulation using a high-order validated model and experimentally using an HiL testbed with a real engine. The electric system is evaluated using a simulation of a high order model. Controllers are designed for automating the operation of diesel and electric wheel loaders to track a given reference cycle in the simulations. The evaluation shows that the optimal cycles produced in previous chapter are reasonable and can be followed closely by the vehicles. Performance of each system relative to the optimal cycle is discussed in detail. Energy consumption predicted by the optimal formulations, the most important part of the

results, is validated with errors of 2.8%, 0.7%, and 6.0% for the diesel simulation, HiL, and electric simulation. Detailed energy flow analysis finds that the electric system energy improvement comes primarily from replacing the engine with a much more efficient battery, along with allowing regenerative braking, removing the torque converter, and splitting the drivetrain and hydraulic circuit onto separate motor shafts.

From this process, recommendations for future work to improve the accuracy and performance of optimal formulations are found: incorporating a constraint on cylinder motion, steering, and main pump speed to ensure sufficient flow for the diesel system; including an estimate of steering energy consumption into the optimization; and incorporating a more dynamic hydraulic efficiency. Further limiting the power demand on the engine would make the system easier to control and follow the reference trajectory, but is not the main factor in tracking errors found in the diesel simulation or experiment. This work further demonstrates the value of systematically designing the optimal control formulation of autonomous wheel loaders, and using additional methods to evaluate the realistic performance of an optimized cycle. Future engineers can use the methodology presented in this chapter to validate and evaluate any reference cycle for a diesel- or electric-powered wheel loader or other similar machine.

Chapter 5

Conclusion and Discussion

5.1 Review

In review, this work presented two trajectory optimization studies and a study on validation and evaluation of optimal trajectories. The optimization studies developed control-oriented models and systematically formulated the multi-objective optimal control problem for a target wheel loader using diesel engine and battery electric power. The evaluation study developed high-order models and automation control architectures for each system with analysis of optimal trajectory-following results.

In Chapter 2, the target diesel wheel loader was introduced with a control-oriented model calibrated using human driving data. The optimal control problem was formulated for this vehicle to optimize both energy efficiency and productivity. A typical drive cycle was defined and converted into boundary constraints for a multi-stage optimization problem to meet the objectives for a cycle. Driving data was used to develop constraints on the state and control variables for a physically realistic optimization setting. This study found:

- Automation and optimization of the diesel wheel loader can lead to 42.1% improvement in fuel consumption per cycle while maintaining or improving productivity.
- The cost function weights of the multi-objective problem can be adjusted to slide between 45.9% increase in fuel efficiency or 11.8% increase in productivity over a human driver as desired.
- Computation time for solving the problem was faster than the time to complete

a cycle, allowing real-time implementation by iteratively re-optimizing the next cycle while completing the current one.

In Chapter 3, a target compact wheel loader was electrified using a battery and two PMSM electric motors to split the drivetrain and hydraulic circuit onto different shafts. Human driving data was used to size parameters for reasonable electric components. A control-oriented model of the electric system was developed for use in optimization. The optimal control problem was systematically formulated with new cost function and constraints based on the electric powertrain, and for a compact version of the diesel wheel loader with a different drive cycle from Chapter 2 for comparison. This study found:

- Automation and optimization of the electric wheel loader can lead to 78% increase in energy efficiency compared to a optimal autonomous diesel wheel loader while matching productivity per cycle.
- A wheel loader with operating weight of 11,000kg and engine power of 120kW can be electrified with a 90kWh battery and two PMSM motors with 120kW and 70kW ratings and match a the daily productivity of a diesel loader with 1.2 battery charges against a human driver and 1.8 battery charger for an optimal autonomous machine.
- The cost function weights of the multi-objective problem can be adjusted to slide between 79% increase in fuel efficiency or 40% increase in productivity over the optimal autonomous diesel vehicle as desired.

In Chapter 4, high order validated models were developed for wheel loaders with both diesel and electric powertrains with focus on energy consuming subsystems. Control architectures were designed to automate operation of the vehicle given a desired trajectory. These together allow for evaluation of any cycle trajectory with detailed information on energy consumption and reference tracking. The diesel vehicle was also validated experimentally using an HiL system with a real engine. This study found:

- The optimal diesel fuel consumption predicted by the optimal solution was within 2.8% of the simulation and 0.7% of the HiL experiment.
- The optimal electric energy consumption predicted by the optimal solution was within 6.0% of the simulation, with the difference accounted for by the steering circuit's energy neglected in the control-oriented model.

- Detailed energy analysis reveals where electrification improves efficiency, including power source efficiency, regenerative braking, removing the torque converter, and separating the drivetrain and hydraulic circuits onto different motors.

5.2 Conclusions

This work provides insight into the potential for improving energy efficiency of wheel loaders and off-highway vehicles in general using automation as a pathway for optimizing their operation.

- Chapter 2 develops a novel formulation of the optimal control problem for an autonomous diesel wheel loader. This gives a process that can be used for automation to improve on human operation, with robustness to variation in modeling parameters, cycle definition, and constraints. This chapter reveals the advantages to optimal automation with regard to the key objectives of energy efficiency and productivity.
- With the systematic formulation shown in Chapter 2, a similar methodology is applied to an entirely new electric powertrain in Chapter 3. This not only demonstrates the huge potential for energy savings through both electrification and automation, but how combining them can extend viability of electric vehicles to a size range beyond the current state-of-the-art without requiring restrictively large electric components.
- 4 evaluates the findings of previous chapters for accuracy and feasibility in an autonomous machine. For optimal results to push off-highway vehicle development towards energy-efficient automation, it is crucial to thoroughly investigate them and motivate the significant technological development automation requires. This chapter also demonstrated the importance of systematically formulating the optimal control problems such that modeling assumptions and constraints can continue to develop to add robustness and adjust to the desired application.

This work suggests that cyclical wheel loader operation can significantly improve energy efficiency through systematic optimization and automation without loss of productivity. Building a mathematical system model with reduced complexity and constraining it to achieve desired objectives within physically realistic bounds is key for developing an

effective formulation. While diesel power is currently used for wheel loaders above the smallest sizes, and can itself be notably improved with automation, this work demonstrates a pathway to using automation to extend electrification further with existing electrical components.

5.3 Recommendations for Future Work

Future work in this area should focus on further exploration of optimal problem development, addressing the technology gaps for automation, and taking steps towards implementing optimal operation.

When optimizing for energy efficiency and production, it is important to focus model fidelity around energy consumption while capturing objective output. Chapters 2 and 3 found that focusing on the core of how subsystems consume energy and neglecting faster dynamics is effective, while evidence provided by Chapter 4 shows incorporating constraints which limit operation within controllable bounds is sufficient to allow actuators to compensate for delays and disturbances induced by neglected dynamics. This recommends future work on incorporating more information into the optimization problem that could impact energy consumption, such as the efficiency of the hydraulic system. While assumed constant for this work, the hydraulic efficiency – primarily main pump efficiency – depends on operating conditions and could be worth the addition of state and/or control variables to approximate it alongside bucket and engine/motor states.

With regard to further development on the control-oriented hydraulic system model, Chapter 4 reveals that steering circuit flow and energy consumption can be important. While small relative to the work circuit and drivetrain, does impact both trajectory tracking performance – especially when all systems are powered by one engine shaft – and overall energy – especially when the rest of the system efficiency is relatively high, as in the electric case. All sets of optimal results emphasize aggressive steering to minimize driving distance with no penalty on the energy it could require. Future work could further develop the flow constraints in the optimal formulation to apply to the diesel system and build an approximation for steering energy with the included states and controls to consider in the energy cost.

With the autonomous control architecture developed in Chapter 4, simple feedback

controllers are sufficient for validation and evaluation but could lack robustness and efficiency in real operation. Future work on optimal controller design that will ensure cycle objectives such as filling the bucket, reaching the dump site, fully lifting the bucket, etc. are achieved while maintaining energy efficiency would ease the pathway towards automation.

With Chapter 3 paving the way for expanding off-highway electrification via optimal automation, a deeper understanding of the interaction between component specifications and cycle objectives is needed. Future work on a sizing study for mid-size electric autonomous wheel loader is supported by this work. It would be valuable to explicitly demonstrate the potential for downsizing electric components for a given machine, find the machine size limit for viability of electrification while using optimal automation, and consider co-optimization of component specifications and cycle trajectory.

Finally, industrial development of autonomous wheel loaders as detailed in this work will take steps to see implemented. HiL experimentation was shown to be effective for validation and obtaining a deeper understanding of desired trajectories for the diesel vehicle. Implementing an HiL system for the electric vehicle with real electric components including the battery, inverters, and motors would be highly desirable for demonstrating the potential for electrification of larger machines. Future work on partial automation would also be useful to push technological development, including driver assistance features and phase-specific automation focused solely on loading, lifting, or way-point transport.

The work of this thesis demonstrates the potential for optimal automation of off-highway vehicle, specifically wheel loaders, to significantly contribute towards reducing energy consumption in the transportation industry. It highlights a method to not only improve operation with automation, but to expand the scope of viable implementation of technology like electrification. The formulations and analysis developed in this work may be used as a reference for future projects around using automation to improve off-highway energy efficiency.

References

[1] CASE. Front end loader 821g | CASE AU.

[2] Lawrence Livermore National Lab. Estimated u.s. energy consumption in 2023. Technical report, DOE.

[3] Lauren Lynch and Bradley T. Zigler. *Estimating Energy Consumption of Mobile Fluid Power in the United States*. Number NREL/TP–5400-70240, 1408087. Nov 2017.

[4] Siddharth Dadhich, Ulf Bodin, and Ulf Andersson. Key challenges in automation of earth-moving machines. *Automation in Construction*, 68:212–222, 2016.

[5] Ahmad Hemami and Ferri Hassani. An overview of autonomous loading of bulk material. In *26th International Symposium on Automation and Robotics in Construction*, pages 405–411, 2009.

[6] Siddharth Dadhich. *Automation of wheel-loaders*. PhD thesis, Luleå University of Technology, 2018.

[7] Guilherme Jorge Maeda. *Learning and Reacting with Inaccurate Prediction: Applications to Autonomous Excavation*. PhD thesis, University of Sydney, 2013.

[8] Carl Borngrund, Fredrik Sandin, and Ulf Bodin. Deep-learning-based vision for earth-moving automation. *Automation in Construction*, 133:104013, 2022.

[9] Siddharth Dadhich, Fredrik Sandin, Ulf Bodin, Ulf Andersson, and Torbjörn Martinsson. Field test of neural-network based automatic bucket-filling algorithm for wheel-loaders. *Automation in Construction*, 97:1–12, 2019.

[10] S. Dadhich, F. Sandin, U. Bodin, U. Andersson and T. Martinsson. Adaptation of a wheel loader automatic bucket filling neural network using reinforcement learning. In *2020 International Joint Conference on Neural Networks (IJCNN)*, pages 1–9, 2020.

[11] R Filla. Optimizing the trajectory of a wheel loader working in short loading cycles. 2013.

[12] Pratap Tokekar, Nikhil Karnad, and Volkan Isler. Energy-optimal trajectory planning for car-like robots. *Autonomous Robots*, 37:279–300, 2014.

[13] Soovadeep Bakshi, Tianheng Feng, Zeyu Yan, Zheren Ma, and Dongmei Chen. Energy-conscientious trajectory planning for an autonomous mobile robot in an asymmetric task space. *Journal of Intelligent & Robotic Systems*, 101:1–14, 2021.

[14] Shaoming He, Chang-Hun Lee, Hyo-Sang Shin, and Antonios Tsourdos. Minimum-effort waypoint-following guidance. *Journal of Guidance, Control, and Dynamics*, 42(7):1551–1561, 2019.

[15] Shuang Liu and Dong Sun. Minimizing energy consumption of wheeled mobile robots via optimal motion planning. *IEEE/ASME Transactions on Mechatronics*, 19(2):401–411, 2013.

[16] V. Nezhadali, L. Eriksson, and A. Fröberg. Modeling and optimal control of a wheel loader in the lift-transport section of the short loading cycle. volume 46, pages 195–200. IFAC Secretariat, 2013.

[17] Vaheed Nezhadali and Lars Eriksson. Optimal lifting and path profiles for a wheel loader considering engine and turbo limitations. *Lecture Notes in Control and Information Sciences*, 455 LNCIS:301–324, 2014.

[18] Vaheed Nezhadali, B Frank, and Lars Eriksson. Wheel loader operation—optimal control compared to real drive experience. *Control Engineering Practice*, 48:1–9, 2016.

[19] Toshinobu Takei, Kentaro Ichikawa, Kazuya Okawa, Shigeru Sarata, Takashi Tsubouchi, and Akira Torige. Path planning of wheel loader type robot for scooping and

loading operation by genetic algorithm. In *2013 13th International Conference on Control, Automation and Systems (ICCAS 2013)*, pages 1494–1499. IEEE, 2013.

[20] Junren Shi, Dongye Sun, Datong Qin, Minghui Hu, Yingzhe Kan, Ke Ma, and Ruibo Chen. Planning the trajectory of an autonomous wheel loader and tracking its trajectory via adaptive model predictive control. *Robotics and Autonomous Systems*, 131:103570, 2020.

[21] Cedric Monnay. Potential and trends in off-highway vehicles' electrification. Technical report, Semcon.

[22] Daniele Beltrami, Paolo Iora, Laura Tribioli, and Stefano Uberti. Electrification of compact off-highway vehicles—overview of the current state of the art and trends. *Energies*, 14(17):5565, Sep 2021.

[23] Hong Wang, Qiang Song, Shengbo Wang, and Pu Zeng. Dynamic modeling and control strategy optimization for a hybrid electric tracked vehicle. *Mathematical Problems in Engineering*, 2015:1–12, 2015.

[24] Yimin Zhao and Yu Wang. Simulation and fuzzy logic analysis on an off-road hev. In *2011 International Conference on Consumer Electronics, Communications and Networks (CECNet)*, page 710–714, Xianning, China, Apr 2011. IEEE.

[25] Dezong Zhao, Richard Stobart, Guangyu Dong, and Edward Winward. Real-time energy management for diesel heavy duty hybrid electric vehicles. *IEEE Transactions on Control Systems Technology*, 23(3):829–841, May 2015.

[26] Hong Wang, Yanjun Huang, and Amir Khajepour. Cyber-physical control for energy management of off-road vehicles with hybrid energy storage systems. *IEEE/ASME Transactions on Mechatronics*, 23(6):2609–2618, Dec 2018.

[27] Iman Shafikhani and Jan Å slund. Energy management of hybrid electric vehicles with battery aging considerations: Wheel loader case study. *Control Engineering Practice*, 110:104759, May 2021.

[28] A. V. Podgornyy, V. V. Filatov, B. S. Subbotin, and P. I. Smirnov. Comparison of the efficiency and energy consumption of an electric wheel loader and a diesel

loader. In *2024 Systems of Signals Generating and Processing in the Field of on Board Communications*, pages 1–6. ISSN: 2768-0118.

[29] Priyatharrshan S Karuppanan. *Autonomous Electrical Wheel Loader - Modelling, Simulation and Evaluation of Efficiency.* phdthesis.

[30] Haoxiang Zhang, Feng Wang, Zichang Lin, and Bing Xu. Optimization of speed trajectory for electric wheel loaders: Battery lifetime extension. 351:121865.

[31] Mohd Azrin Mohd Zulkefli, Pratik Mukherjee, Zongxuan Sun, Jianfeng Zheng, Henry X. Liu, and Peter Huang. Hardware-in-the-loop testbed for evaluating connected vehicle applications. *Transportation Research Part C: Emerging Technologies*, 78:50–62, May 2017.

[32] Yunli Shao, Mohd Azrin Mohd Zulkefli, Zongxuan Sun, and Peter Huang. Evaluating connected and autonomous vehicles using a hardware-in-the-loop testbed and a living lab. *Transportation Research Part C: Emerging Technologies*, 102:121–135, May 2019.

[33] Allan J. Kotwicki. Dynamic models for torque converter equipped vehicles. *SAE Technical Papers*, 2 1982.

[34] Zongxuan Sun and Guoming G. Zhu. *Design and control of automotive propulsion systems.* CRC Press, 1 2014.

[35] Yunli Shao and Zongxuan Sun. Robust eco-cooperative adaptive cruise control with gear shifting. *Proceedings of the American Control Conference*, pages 4958–4963, 6 2017.

[36] A. R. Reece. Paper 2: The fundamental equation of earth-moving mechanics. *Proceedings of the Institution of Mechanical Engineers, Conference Proceedings*, 179(6):16–22, 1964, https://doi.org/10.1243/PIME_CONF_1964_179_134_02.

[37] Sencheng Yu, Xingyong Song, and Zongxuan Sun. On-line prediction of resistant force during soil-tool interaction. 56(3):133–138.

[38] Joel A E Andersson, Joris Gillis, Greg Horn, James B Rawlings, and Moritz Diehl. CasADi – A software framework for nonlinear optimization and optimal control. *Mathematical Programming Computation*, 11(1):1–36, 2019.

[39] Andreas Wächter, Lorenz, and T Biegler. Digital object identifier (on the implementation of an interior-point filter line-search algorithm for large-scale nonlinear programming. *Math. Program., Ser. A*, 106:25–57, 2006.

[40] Anil V. Rao, David A. Benson, Christopher Darby, Michael A. Patterson, Camila Francolin, Ilyssa Sanders, and Geoffrey T. Huntington. Algorithm 902: Gpops, a matlab software for solving multiple-phase optimal control problems using the gauss pseudospectral method. *ACM Transactions on Mathematical Software*, 37, 4 2010.

[41] Philip Polack, Florent Altché, Brigitte d'Andréa Novel, and Arnaud de La Fortelle. The kinematic bicycle model: A consistent model for planning feasible trajectories for autonomous vehicles? In *2017 IEEE Intelligent Vehicles Symposium (IV)*, pages 812–818, 2017.

[42] M. Abul Masrur. Hybrid and electric vehicle (hev/ev) technologies for off-road applications. *Proceedings of the IEEE*, 109(6):1077–1093, Jun 2021. Publisher: Institute of Electrical and Electronics Engineers Inc.

[43] Carlo Cunanan, Manh-Kien Tran, Youngwoo Lee, Shinghei Kwok, Vincent Leung, and Michael Fowler. A review of heavy-duty vehicle powertrain technologies: Diesel engine vehicles, battery electric vehicles, and hydrogen fuel cell electric vehicles. 3(2):474–489. Number: 2 Publisher: Multidisciplinary Digital Publishing Institute.

[44] Ali Emadi. *Advanced electric drive vehicles.* Energy, power electronics, and machines series. CRC Press, Taylor & Francis Group, Boca Raton, Florida, 2015.

[45] Sencheng Yu, Xingyong Song, and Zongxuan Sun. On-line prediction of resistant force during soil–tool interaction. 145(81004).

[46] Gaonan Zhao, Connor P Edson, Jie Yao, Zongxuan Sun, and Kim A Stelson. Development of a dynamical model and energy analysis for wheel loader. page 09544070231188772.

[47] Gaonan Zhao, Jie Yao, Connor P. Edson, and Zongxuan Sun. Design, modeling, and control of a hardware-in-the-loop testbed for off-road vehicles1. 4(41003).

[48] Kumaraswamy Hebbale, Chunhao Lee, Farzad Samie, Chi Kuan Kao, Xu Chen, Jeremy Horgan, and Scott Hearld. Model based torque converter clutch slip control. In *SAE 2011 World Congress and Exhibition*. ISSN: 0148-7191.

[49] Sencheng Yu, Gaonan Zhao, Xingyong Song, and Zongxuan Sun. Control oriented model order reduction for the hydraulic system of an autonomous wheel loader. 139:105628.

[50] R. H. Park. Two-reaction theory of synchronous machines generalized method of analysis-part i. 48(3):716–727. Conference Name: Transactions of the American Institute of Electrical Engineers.

[51] Myungwook Park, Sangwoo Lee, and Wooyong Han. Development of steering control system for autonomous vehicle using geometry-based path tracking algorithm. 37(3):617–625. Publisher: ETRI.

[52] Noor Hafizah Amer, Hairi Zamzuri, Khisbullah Hudha, and Zulkiffli Abdul Kadir. Modelling and control strategies in path tracking control for autonomous ground vehicles: A review of state of the art and challenges. 86(2):225–254. Publisher: Springer Netherlands.

[53] Ravindra Kumar Sharma, Vivek Sanadhya, Laxmidhar Behera, and S. Bhattacharya. Vector control of a permanent magnet synchronous motor. In *2008 Annual IEEE India Conference*, volume 1, pages 81–86. ISSN: 2325-9418.

Appendix A

Model Parameters and Specifications

This appendix summarizes the parameters and specifications used in each model. Model values are pulled from directly relevant data sheets and/or curve fits to data when available, and otherwise set to reasonable values based on literature and related data sheets.

A.1 Control-Oriented Model Parameters

Symbol	Value	Unit	Description
T_{bp}	50	Nm	Brake pump torque
J_e	8	$kg-m^2$	Engine shaft inertia
η_e	0.4722	–	Engine combustion efficiency
q_{hv}	42.9	MJ/kg	Diesel fuel heat value
n_{cyl}	6	–	Number of engine cylinders
V_d	0.0067	m^3	Engine displacement volume
c_1	$-3.8*10^{-4}$	kg/m	Engine coulomb friction coefficient
c_2	0.1155	$kg-s/m$	Engine viscous friction coefficient
c_3	-4.8766	$kg-s^2/m$	Engine dry friction coefficient
a_1	$1.7*10^{-4}$	$kg-m^2/rad$	TC pump torque coefficient
a_2	$9.9*10^{-5}$	$kg-m^2/rad$	TC pump torque coefficient
a_3	$-1.6*10^{-4}$	$kg-m^2/rad$	TC pump torque coefficient
b_1	$4.3*10^{-4}$	$kg-m^2/rad$	TC turbine torque coefficient
b_2	$-3.1*10^{-4}$	$kg-m^2/rad$	TC turbine torque coefficient
b_3	$-9.6*10^{-5}$	$kg-m^2/rad$	TC turbine torque coefficient
C	50	–	Shift schedule steepness
J_d	19	$kg-m^2$	Driveshaft inertia
R_w	0.761	m	Wheel radius
k_f	24.67	–	Final drive ratio
μ	0.0455	–	Rolling friction coefficient
m	18170	kg	Vehicle mass
g	9.8	m/s^2	Gravitational acceleration
R_b	1	m	Bucket center of mass radius
ψ	10	deg	Bucket angle differential
m_b	1537	kg	Bucket mass (empty)
m_{load}	5900	kg	Material mass for full bucket
η	0.9	–	Hydraulic circuit efficiency
L	3.34	m	Vehicle wheelbase length
τ_s	0.06	s	Steering circuit time constant
K_s	1	–	Steering circuit gain
$T_{e,max}$	850	Nm	Engine maximum torque
$T_{mp,max}$	315	Nm	Main pump maximum torque
N_{steps}	15	–	Time steps for each stage
d	3	–	Order of Lagrangian collocation polynomial

Table A.1: Diesel vehicle modeling parameters used in Chapter 2

Symbol	Value	Unit	Description
T_{bp}	25	Nm	Brake pump torque
J_e	4	$kg-m^2$	Engine shaft inertia
η_e	0.4089	–	Engine combustion efficiency
q_{hv}	42.9	MJ/kg	Diesel fuel heat value
n_{cyl}	4	–	Number of engine cylinders
V_d	0.0067	m^3	Engine displacement volume
c_1	$5.7*10^{-5}$	kg/m	Engine coulomb friction coefficient
c_2	-0.0133	$kg-s/m$	Engine viscous friction coefficient
c_3	1.4328	$kg-s^2/m$	Engine dry friction coefficient
a_1	$9.2*10^{-5}$	$kg-m^2/rad$	TC pump torque coefficient
a_2	$1.3*10^{-4}$	$kg-m^2/rad$	TC pump torque coefficient
a_3	$-2.0*10^{-4}$	$kg-m^2/rad$	TC pump torque coefficient
b_1	$2.3*10^{-4}$	$kg-m^2/rad$	TC turbine torque coefficient
b_2	$-5.8*10^{-5}$	$kg-m^2/rad$	TC turbine torque coefficient
b_3	$-1.7*10^{-4}$	$kg-m^2/rad$	TC turbine torque coefficient
C	50	–	Shift schedule steepness
J_d	30	$kg-m^2$	Driveshaft inertia
R_w	0.703	m	Wheel radius
k_f	13.46	–	Final drive ratio
μ	0.0455	–	Rolling friction coefficient
m	11018	kg	Vehicle mass
g	9.8	m/s^2	Gravitational acceleration
R_b	1	m	Bucket center of mass radius
ψ	60	deg	Bucket angle differential
m_b	700	kg	Bucket mass (empty)
m_{load}	1500	kg	Material mass for full bucket
η	0.45	–	Hydraulic circuit efficiency
L	2.75	m	Vehicle wheelbase length
τ_s	0.06	s	Steering circuit time constant
K_s	1	–	Steering circuit gain
$T_{e,max}$	510	Nm	Engine maximum torque
$T_{mp,max}$	170	Nm	Main pump maximum torque
$T_{load,max}$	400	Nm	Engine total load maximum torque
$N_{transport}$	15	–	Time steps for each transport stage
$N_{loading}$	25	–	Time steps for each loading stage
d	3	–	Order of Lagrangian collocation polynomial

Table A.2: Compact diesel vehicle modeling parameters used in Chapters 3 & 4

Symbol	Value	Unit	Description
E_{nom}	90	kWh	Battery energy capacity
V_{nom}	800	V	Battery voltage
R_{bat}	1	Ω	Battery resistance
I_{max}	300	A	Motor current limit
Φ_d	0.386	Wb	Drive motor magnetic flux strength
Φ_h	0.2205	Wb	Hydraulic motor magnetic flux strength
P_p	4	$pairs$	Motor pole pairs
L_q	0.0032	H	Motor q-axis inductance
L_d	0.0017	H	Motor d-axis inductance
R_s	0.02	Ω	Motor winding resistance
J_d	0.085	$kg-m^2$	Drive motor inertia
J_h	0.05	$kg-m^2$	Hydraulic motor inertia
b_d	0.01	$N-m-s/rad$	Drive motor friction coefficient
b_h	0.01	$N-m-s/rad$	Hydraulic motor friction coefficient
$P_{max,d}$	121.6	kW	Drive motor maximum power
$P_{max,h}$	69.7	kW	Hydraulic motor maximum power
$P_{max,em}$	160	kW	Total maximum motor power
$\gamma_{t,1}$	10	–	Transmission gear ratio, 1st gear
$\gamma_{t,2}$	3	–	Transmission gear ratio, 2nd gear
γ_h	2	–	Hydraulic shaft fixed gear ratio
p_1	0.0214	–	Loss electrical coefficient
p_2	0.0084	–	Loss mechanical coefficient
p_3	0.0359	–	Loss shaft power coefficient
p_4	0	–	Loss constant coefficient
D_{mp}	0.0113	L/rad	Main pump maximum displacement
A_{lift}	0.0162	m^2	Lift cylinder area
A_{tilt}	0.0103	m^2	Tilt cylinder area
p_l	0.225	–	Lift velocity coefficient
p_t	0.3175	m/rad	Tilt velocity coefficient
p_s	0.0011	m^3/rad	Steering flow coefficient
p_{b1}	1.838	$1/m$	Bucket quadratic spacial coefficient
p_{b2}	1.293	–	Bucket linear spacial coefficient
p_{b3}	-0.2056	m	Bucket constant spacial coefficient
$N_{transport}$	75	–	Time steps for each transport stage
$N_{loading}$	25	–	Time steps for each loading stage
d	3	–	Order of Lagrangian collocation polynomial

Table A.3: Electric vehicle modeling parameters used in Chapters 3 & 4